Effects of Rare Earths on Microstructure and Wear Resistance in Metal Additive Manufacturing: A Review

Dingding Xiang [1,2,3,*], Di Wang [1], Tingfang Zheng [1] and Yu Chen [1]

1   School of Mechanical Engineering and Automation, Northeastern University, Shenyang 110819, China; wxd_990511@163.com (D.W.); a1924917689@163.com (T.Z.)
2   State Key Laboratory of Solid Lubrication, Lanzhou Institute of Chemical Physics, Chinese Academy of Sciences, Lanzhou 730000, China
3   Foshan Graduate School of Innovation, Northeastern University, Foshan 528311, China
*   Correspondence: xiangdd@mail.neu.edu.cn

Abstract: Rare earth elements (REEs) doping technology can effectively control the microstructure and improve the quality and performance of materials. This paper summarizes the research progress of REEs in metal additive manufacturing (MAM) in recent years and briefly introduces the effects of REEs on the molten pool fluidity, purified structure, and interfacial bonding between the molten cladding layer and substrate. It focuses on the mechanism of the role of REEs in the refinement and homogenization of microstructures, including grain growth, columnar to equiaxed transition (CET), and elemental segregation. The reasons for the influence of REEs on the homogenization of the structure and elemental segregation are analyzed. The effects of REE type, content, and dimension on hardness and wear resistance are investigated. Finally, tribological applications of REEs in biological and high-temperature environments are summarized, and the impact of REEs-modified alloys is summarized and prospected.

Keywords: additive manufacturing; rare earth elements; microstructure; wear resistance; a review

1. Introduction

Additive manufacturing (AM), known as 3D printing technology, is a method of fabricating materials layer by layer based on a three-dimensional computer-aided design model [1–3]. The method improves productivity, minimizes waste materials, and permits the manufacture of complicated geometric pieces. However, each layer of material deposition in the AM technique undergoes a complex thermal process. This temperature field results in the formation of multiscale microstructures in the molten pool, which has a significant impact on the material's hardness, wear resistance, and corrosion resistance [4–8]. Microstructural inhomogeneity along the deposition direction was observed during the AM process by Wang et al. [9], which can be attributed to different cooling rates and multiple heating cycles between layers. The top layer is characterized by well-developed dendrites covered by an eutectic structure, while the bottom part consists of small grains containing precipitates. The mechanics and lifetime of the materials are impacted by the microstructural inhomogeneity, which results in variations in the material properties. Some academics have proposed mixing rare earth elements (REEs) in raw material powders to solve the issue of property anisotropy caused by microstructure in metal additive manufacturing (MAM).

The 17 elements that constitute REEs exhibit physical characteristics such as large atomic radii, unique electronic structures, and excellent chemical activity [10,11]. REEs include Sc, Y, and the lanthanides, which are La, Ce, Pr, Nd, Pm, Sm, Eu, Gd, Tb, Dy, Ho, Er, Tm, Yb, and Lu [12,13]. As shown in Figure 1, REEs are introduced in the types of rare earth oxides (REOs: CeO_2, La_2O_3, and Y_2O_3), rare earth halides (YF$_3$, CeCl$_3$, and LaF$_3$), rare earth borates (LaB$_6$, CeB$_6$, and ErB$_4$), rare earth nitrogen/carbide (REN/REC: LaN, CeC$_2$, and GdN), and pure REEs. Due to their unique properties, REEs make an important

contribution to improving energy efficiency, reducing harmful emissions, and enhancing the performance of materials. REEs are widely used in many fields, including new energy technologies [14], magnetic materials [15], catalysts [16], and optical glass [17]. The mechanisms of REE in the MAM have not been fully clarified, so the study of rare earths in material modification still requires further research and exploration.
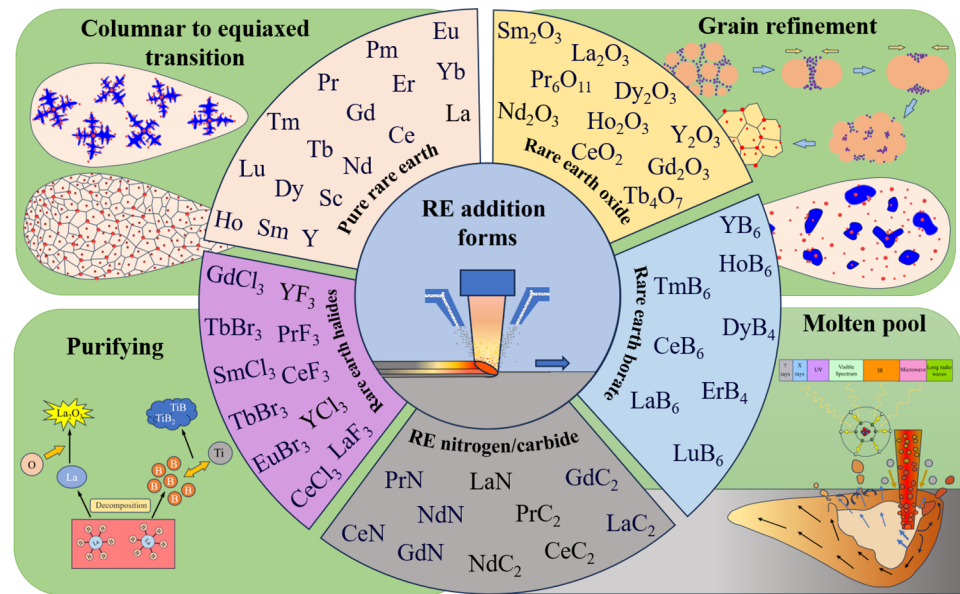

Figure 1. REEs incorporation formats and reinforcement mechanisms in MAM processes.

During the solidification of MAM, appropriate REEs can accomplish grain refinement, liquid-phase metal purification, inclusion improvement, and structure homogenization. These effects can reduce the materials' cracking susceptibility while increasing the alloys' hardness, wear resistance, and corrosion resistance. Furthermore, REEs have significant effects on the solidification and phase transition behavior of alloys, which improve the microstructure and mechanical properties of MAM materials to enhance reliability and service life.

This paper summarizes the research progress of REEs in MAM in recent years and briefly introduces the effects of REEs on the molten pool fluidity, purified structure, and interfacial bonding between the molten cladding layer and the substrate. It focuses on the mechanisms of the role of REEs in the refinement and homogenization of microstructures, including grain growth, columnar to equiaxed transition (CET), and elemental segregation. The reasons for the influence of REEs on the homogenization of the structure and elemental segregation are analyzed. The effects of REE type, content, and dimension on hardness and wear resistance are investigated. Finally, tribological applications of REEs in biological and high-temperature environments are summarized, and the impact of REEs-modified alloys is summarized and prospected.

2. Macroscopic Effect of REEs in MAM Processes

REEs are an important strategic resource with unique physical and chemical properties that have been particularly studied and applied in the fields of materials science and engineering. Many scholars have researched the effects of REEs in a variety of material processing and preparation processes in anticipation of optimizing processes and improving product quality in metalworking, metallurgy, and other fields.

2.1. Effect of REEs on Molten Pool Mobility

The molten pool fluidity is the ability of the molten metal to flow during the solidification process, which is important for the solidification structure and mechanical properties of alloys. REEs, as doping elements, change the solidification behavior of metals and affect

the molten pool fluidity. Therefore, the study of REEs on molten pool fluidity contributes to the understanding of the solidification process of alloys and provides a theoretical basis for the design and preparation of metallic materials.

2.1.1. Increased Laser Absorption in the Molten Pool

With their unique electrical structure and broad absorption spectrum, REEs can be used to increase the absorption of laser energy on metal powder surfaces. REEs have a broad absorption spectrum that absorbs various wavelengths of light, facilitating energy transfer between the laser and the powder. As illustrated in Figure 2, laser irradiation triggers electrons in REEs to transition from high energy levels to low energy levels, which increases the laser absorption rate of powder [18,19]. Yang et al. [20] discovered that Y_2O_3 boosted the cladding layer's energy density, raising the molten pool temperature over the melting point of WC particles and increasing the concentration of W atoms within the cladding layer. The melting depth of the Ti-based coatings increased from 1188 μm to 1548 μm and was subsequently reduced to 1482 μm as the content of CeO_2 increased [21].
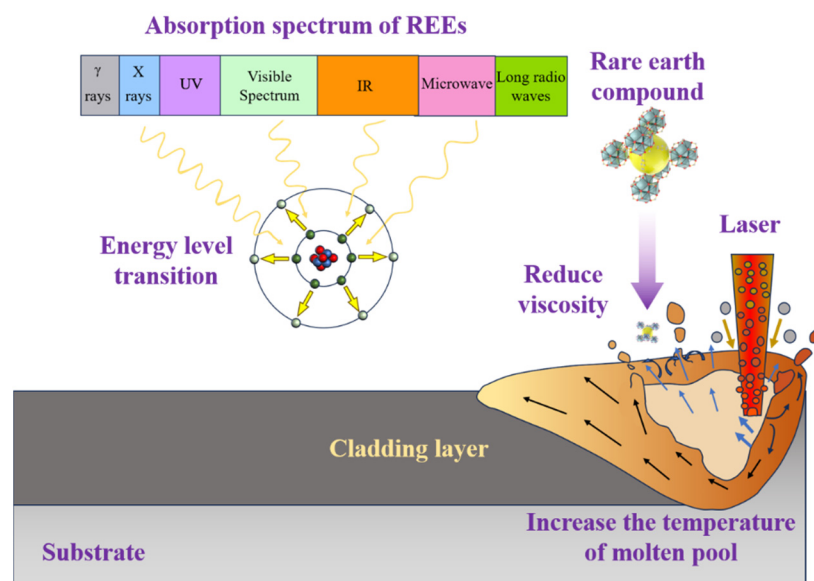

Figure 2. Mechanism of REEs to facilitate molten pool mobility.

The excellent interfacial properties of REEs improve the wettability of the alloy surface, resulting in higher absorption of laser irradiation energy on the surface of powders [22]. When laser cladding the WC-reinforced coatings with varied REO contents on Invar steel, Du et al. [23] reported that Y_2O_3 increased the laser absorption of powders and the weldability of Invar steel, which in turn raised the thickness of the coatings. In the process of laser cladding, REEs have a significant effect on improving the mobility of the molten pool. REEs have high vapor pressure and low oxidizability, which can reduce the surface tension of the molten pool and promote the flow and wetting of molten metal. In addition, REEs can reduce viscosity, minimize intermolecular friction, and improve flow by altering the chemical bonding and molecular structure of the molten pool. The synergistic effect of the above mechanisms enables the REEs to significantly improve the fluidity of the molten pool during the MAM and optimize the structure and properties of the alloys.

2.1.2. Decrease in Surface Tension in the Molten Pool

Due to the Gaussian distribution of laser power in MAM, there is a huge temperature difference between the center and the border of the molten pool, which results in the Marangoni effect. REEs change the surface tension gradient in the molten pool, affecting the velocity and direction of the Marangoni flow. When the CeO_2 content is less than 0.6 wt.%, the surface tension coefficient of the molten pool is positive, the flow center

oscillates around its geometrical center, and an unstable connection line forms between the cladding layer and the substrate [24]. When the CeO_2 concentration is above 0.6 wt.%, the surface tension decreases, the junction line is more stable, and the molten pool flows outward from the center and inward from the periphery. He et al. [25] showed that two vortexes created from the perimeter to the center were generated on both sides of the HEA composite coatings with REEs. As the REE content increases, the vortex gradually expands to both sides, which results in a more stable junction line, as shown in Figure 3. In summary, the Marangoni effect in the molten pool seriously affects the shape and quality of the cladding layer.
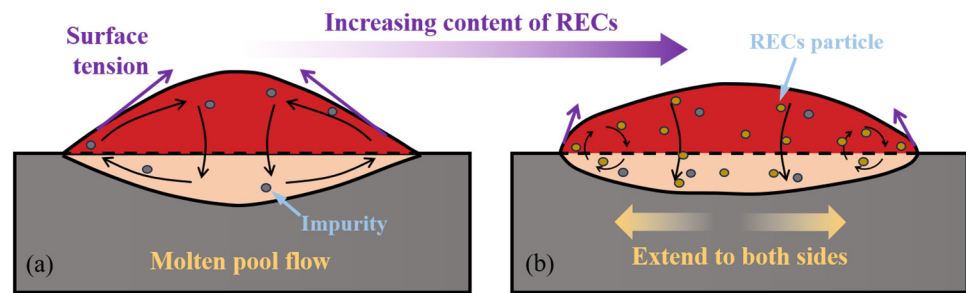

Figure 3. Effect of RECs on Marangoni flow in a molten pool without (**a**) and with RECs (**b**).

Wettability is used to evaluate the mobility of the metal elements in the molten pool. REEs can reduce the surface tension of the alloy, making the alloy more wettable. A high-fluidity molten pool is beneficial to the diffusion of alloying elements, improving the alloy's mechanical characteristics and wear resistance. In the existing research, the surface tension and the wetting angle of the molten pool are often employed to determine mobility. The calculation formula is as follows:

$$cos\,\theta = \frac{\gamma_{sl} - \gamma_{sg}}{\gamma_{lg}} \tag{1}$$

where γ_{sl}, γ_{sg}, and γ_{lg} are the surface tensions at the solid–liquid interface, solid–gas interface, and liquid–gas interface, respectively, and θ is the wettability of the liquid to the solid surface. When θ is between 0 and 90°, the liquid–solid phase's wettability contributes to interfacial diffusion, resulting in a lower surface tension; when θ is greater than 90°, the liquid–solid phase is not completely wet, resulting in a higher surface tension. Shu et al. [26] identified Ce as a typical surfactant to reduce surface tension, thereby improving wetting angle and promoting liquid metal fluidity. Liu et al. [27] produced Ti-based composite coatings enhanced with CeO_2 on the surface of the Ti811 alloy. CeO_2 interacts with Ti_2Ni to generate a Ti-Ce phase with a low melting point and great wettability, which increases molten pool movement and eliminates herringbone cracks in the coatings. This improves cladding layer surface quality.

The viscosity, laser absorption, and surface tension of the material have a substantial impact on the mobility of the molten pool. REE's unique electronic structure and low surface energy not only boost the rate of laser absorption but also produce well-wetting compounds that minimize surface tension. The greater mobility makes it possible for the molten cladding layer to develop a metallurgical bond with the substrate more easily, decreasing the formation of defects like pores and cracks. In practice, according to the specific alloy composition and manufacturing conditions, reasonable proportions and controls are carried out to optimize the benefits of REE and achieve excellent cladding quality.

2.2. Effect of REEs on the Purity of the Molten Pool

2.2.1. REEs Purify the Molten Pool of Impurity Metals

MAM alloys consist of a low concentration of hazardous metal elements (such as Cu, Fe, and Mn), which hurts the alloy's performance. REEs interact with these elements to form stable compounds that can purify the molten pool. The rare earth atoms (REAs) react

chemically with metal impurity atoms in the molten pool to produce stable RECs. For example, La, Ce, Y, and Er promote the formation of compounds such as La_5Si_3, $CeFe_2Si_2$, YSiFe, and $Er_{1.2}Fe_4Si_{9.8}$ [28,29], which are expelled as slag. Ding et al. [30] demonstrated that the addition of Y reduced impurities in the Fe-rich phase at the grain boundary, contributing to the purity of the alloy.

When Y_2O_3 is added to the molten pool of Ti-based alloys, it is dissolved in the form of Y_2O_3 (solid) $\rightarrow$ Y + O (molten). In the molten state, the Y and O atoms make strong combinations with substrate elements and are prone to generating intermetallic compounds, which serve to purify the molten pool [31]. Both Er and Pr can purify liquid aluminum and minimize the remaining phases. The purification effect of Pr is better than Er [32], significantly enhancing the alloy's comprehensive performance. According to electronegativity studies of REEs and substrate elements, the decomposition of RECs in the molten pool produces REAs. These atoms prefer to react with elements (such as Al, Fe, and Mn) to generate stable compounds, purifying the composition of the molten pool in the MAM process.

2.2.2. REEs Purify the Molten Pool of Non-Metallic Impurities

Non-metallic elements (P, S, H, O, C, and N) in MAM react with metal elements during solidification, causing lattice defects, phase transitions, and the production of brittle phases, thereby reducing the mechanical and tribological properties of the alloys. REEs can react with these harmful elements to form stable RECs, which are expelled during the solidification process, significantly reducing the concentration of harmful elements in the alloy. The reaction order of REEs with potential inclusion-forming elements should be O, S, As, P, and C [33]. The addition of Ce reduces the concentrations of S and Se in HEAs from 46 ppm and 105 ppm to 22 ppm and 80 ppm, respectively, along with a decrease in the quantity and area of inclusions [34]. Chen's studies showed Ce can react with impurity elements (S, O, B, and Si) to generate high melting point compounds, which will float out of the molten alloy by convection [35]. Weng et al. [36] found that a few Y_2O_3 decomposed into O atoms, which reacted with B and Si in the Co42 self-fluxing alloy to form low-density oxidation products floating on the surface of the molten pool.

REAs react with oxygen atoms in the molten pool to generate REOs, which are reinforced phases and reduce the oxygen concentration. LaB_6 decomposes in the molten pool as $LaB_6 \rightarrow La + 6B$. The La element has a strong reaction on O atoms to generate La_2O_3 [37], and the B element combines with Ti to generate TiB and TiB_2. The La and Ti elements are uniformly distributed in the substrate, and B elements are concentrated in the white precipitates, as shown in Figure 4a–d [38]. According to Liu's study [39], 718H steel coatings decreased total oxygen concentration from 15 ppm to 6 ppm, and Ce + La content increased to 0.022 wt.%. Without LaB_6, Feng et al. [40] noticed that O atoms exist in titanium matrix composites (TMCs) in solid or free form. The oxygen atoms were uniformly distributed, as shown in Figure 4f. When 3.0 wt.% LaB_6 was added to the TMCs, the oxygen element aggregated at points A and B of the coating, as shown in Figure 4e. It was identified as La_2O_3 using XRD. Decreased oxygen concentration enhances molten pool purity, which contributes to the elimination of impurity defects and improves the quality of the cladding layer.

Excessive doping of REEs in MAM alloys produces hard phase particles and intermetallic compounds, which increase the susceptibility to brittleness and microcracking [41]. Particularly, REEs combine with the non-metallic elements in the molten pool to form gas. For example, CeO_2 reacts with the elements C, S, and W in the molten metal to produce CO, SO_2, and W_2O_3 and other gases [26]. These gases cause bubbles to emerge in the molten alloys, which increases the number of pores and decreases the densification of the cladding layers. Therefore, the addition of REEs should be strictly controlled in the MAM process to avoid excessive hazards.

In summary, the appropriate amount of REEs in the MAM process can effectively purify the inclusions and metal impurities in the molten pool to improve the performance

and quality of alloys. REEs react with metallic impurities (Cu, Fe, and Mn) to generate compounds, which are eliminated as slag during solidification. In addition, REEs react with non-metallic elements (P, S, H, O, C, and N) to create RECs with stable melting points, which can be removed from the liquid metal molten pool by upwelling at lower temperatures.
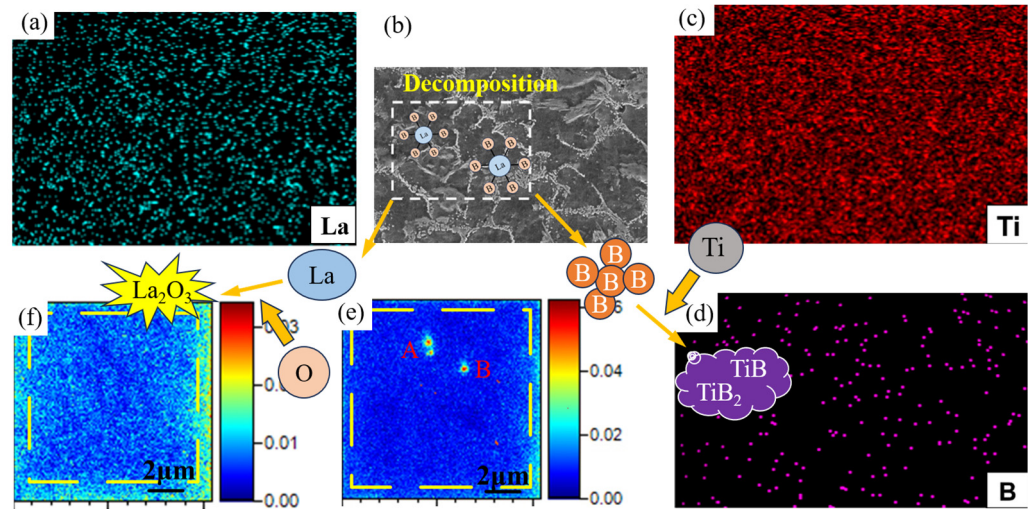

Figure 4. Distribution of La (**a**), Ti (**c**) and B (**d**) elements in LaB_6-modified TC4 (**b**) [38]; the O concentrations of TMCs with 3.0% LaB_6 (**e**) and 0% LaB_6 (**f**) [40]. Reprinted with permission from Ref. [38], 2023, MDPI and Ref. [40], 2019, ELSEVIER.

2.3. Effect of REEs on Interfacial Bonding

2.3.1. Improvement of Molten Pool Dilution Rate

The molten pool dilution rate is the degree of change in the composition of the cladding alloy caused by the molten substrate material mixing [42]. Figure 5 depicts the flow model of the molten pool cross-section and the formula for calculating the dilution rate in MAM. REEs can efficiently lower the dilution rate [43] and improve metallurgical bonding between the cladding layer and the substrate. He et al. [25] discovered that CeO_2 lowers molten pool viscosity. The coating dilution reduced from 72.57% to 32.18% and then climbed to 50.65% as the CeO_2 concentration in HEA increased. Chen et al. [44] analyzed the trends of major elements in the transition zone of coatings with varied CeO_2 concentrations and discovered that CeO_2 increased the fusion latent heat of coatings while inhibiting the diffusion of alloying elements (Cr, Fe, and Co). New compounds, Ce_2Co_{17} and $Ce_6Ni_7Si_4$, were generated at the contact interface, which increased the interfacial bond strength.

The shape of the fusion line between the cladding and the substrate is also affected by the dilution rate. The fusion line is irregularly wavy due to the surface tension of the molten pool and the surface elasticity of the substrate during solidification. A straight fusion line implies a poor metallurgical bonding capacity because the substrate surface is not well-melted. Zhang et al. [45] discovered that when Sc concentration increases, the alloy with 0.3 wt.% Sc has a steeper curved fusion line, and the shear strength of the interface is 48% higher than the alloy without Sc. Zhang et al. [46] discovered that as the La_2O_3 concentration increases, the curvature of the fusion line increases, showing that the REOs enhance metallurgical bonding between the substrate and the coatings.

Moderate amounts of REEs effectively improve molten pool fluidity, but excessive REEs generate considerable steady-state compounds with substrate elements that affect the dilution rate. A low dilution rate results in poor bonding performance between the cladding layer and the substrate and even fails to realize metallurgical bonding. The higher the dilution rate, the greater the degree of mixing between the cladding layer and the substrate, and the stronger the interfacial bond. However, the excessively high dilution rate will diminish the hardness of the substrate's molten zone and the cladding material system, which produces a large stress gradient and leads to cracking.
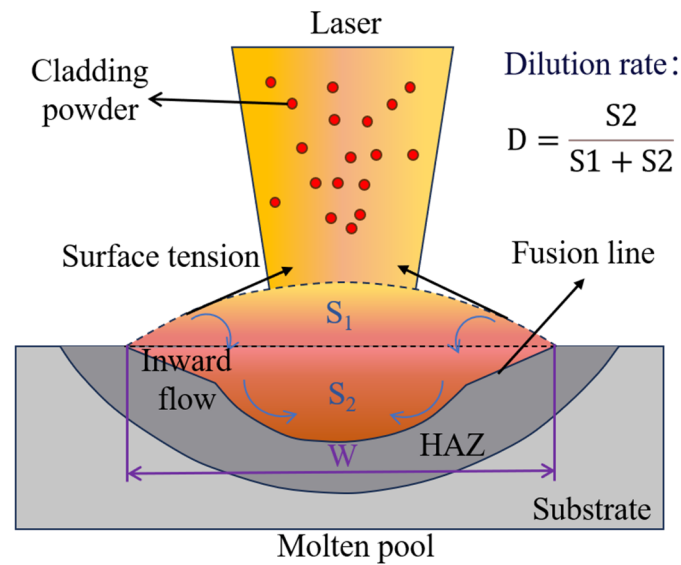
Figure 5. Molten pool structure diagram of laser cladding.

2.3.2. Promotion of Interfacial Chemical Bond Formation

Many vacant orbitals found in REEs can coordinate with elements with the lone electron pairs at the contact interface, resulting in strong interfacial chemical interactions. Zhang et al. [47] discovered that Ce and La were preferentially segregated at the interface, promoting the formation of Cr–C bonds and thereby increasing the interfacial bond strength between diamonds and alloys. Sm increases Cr diffusion in the substrate, promoting the formation of interfacial chromium carbides (Cr_3C_2 and Cr_7C_3) [48]. The highly active Yb atoms at the solid/liquid boundary reacted with the Al atoms of the substrate to generate Al_3Yb compounds that operated as 'bridge' [49]. It connects the cladding layer to the substrate, resulting in a stronger interface connection. The study by Jiang [50] revealed Ce could generate coordination connections at the interface between titanium alloy and resin based on density functional theory, as shown in Figure 6a, which improves the surface wettability of the substrate and the penetration and physical adhesion of the PEEK to the titanium alloy. During the cladding process, when the cladding material contacts the substrate material, atoms or molecules interact and form new interfacial chemical bonds. If the interfacial bonds are strong enough, the bonding between the cladding and the substrate will be significantly enhanced, thus improving adhesion and comprehensive performance.

Many scholars have investigated the doping interface energy (DIE), doping formation energy (DFE), and solution energy (SE) using first principles to determine the mechanism of REEs in the interface bonding process. Generally, the smaller the values of the above three energies, the more stable the interfacial bonding. By doping REEs (Sc, Y, La, Pr, Nd, Eu, Gd, and Dy) in C-BS-Fe alloys, Zhang et al. [51] discovered that when Nd atoms were substituted for Fe atoms, the DFE was negative, and the interfacial structure was the most stable. Fe–Cr, Nd–C, Fe–Nd, and Nd–C bonds were generated at the mushy zone; the fundamental principle is shown in Figure 6c,e, increasing the interfacial bond strength. Li et al. [52] observed that the DIE of doped Nd, Y, Ce, and La reduced from 3.586287 J/m^2 to negative values, and the DFE also decreased to negative values. Furthermore, when REAs replace Fe atoms, the interfacial energy is lower, and the interfacial bonding is more stable than when Ti atoms are replaced. Among the above four REEs, Ce has the most noticeable effect on the characteristics of TiC/Fe composites.

REEs contribute to charge transfer and electrical interactions at the interface, which is the main reason for the higher interfacial bond strength. Yan et al. [54] demonstrated that during the interface-building process, the outermost electrons of the REAs hybridized with the Fe-s, Fe-p, Fe-d, B-s, and B-p orbital electrons, which improved the ionic bonding capabilities in the doped interfaces. When Y atoms replace Fe atoms, the electrons around

Y and Fe create new chemical bonds, increasing the stability of the interfacial bonding. Shi et al. [53] studied the bonding of the REEs (Sc, Y, and La)-doped Cu/graphene interface, as shown in Figure 6b, where a numerous charge exists between the REAs and the graphene, which is more than the undoped REEs. Furthermore, charge accumulation between the REEs and the Cu atoms strengthens the interfacial interbonding. The La-doped interface shows a significant increase in charge accumulation compared to the other two doped interfaces, increasing the strength of interfacial bonding in the order of La > Y > Sc.
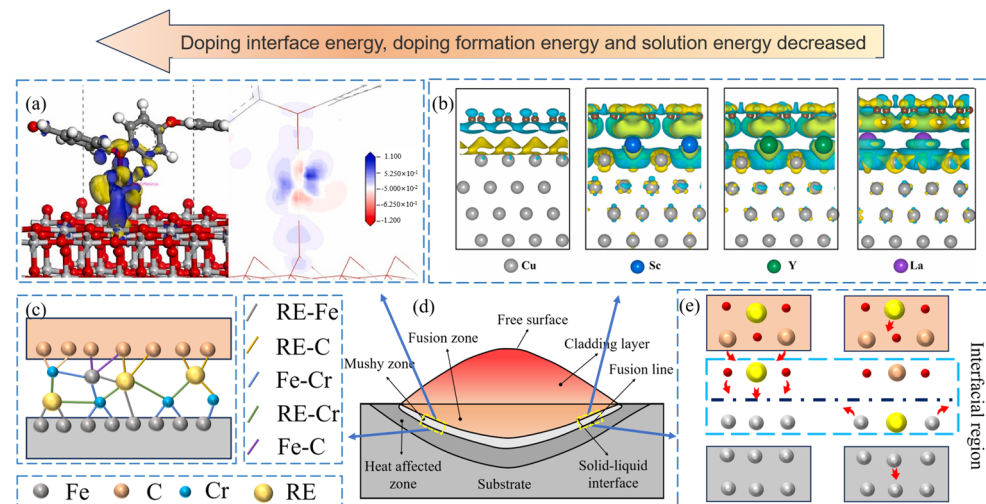

Figure 6. Schematic diagram of REEs promoting chemical bonding in the bonding zone; (**a**) is the EDD mapping of the interface of TiO_2 and PEEK [50], (**b**) is the differential charge density of different interfaces [53], (**d**) is the cross-sectional structure of the cladding layer, and (**c**,**e**) is the mechanism of REEs to promote atomic exchange at the interface. Reprinted with permission from Ref. [50], 2023, ELSEVIER and Ref. [53], 2022, ELSEVIER.

In summary, the high-energy laser beam melts the substrate and the cladding material to form a mushy zone where the substrate and the cladding material are mixed and chemically react to form chemical bonds in laser cladding [55]. These bonds include metallurgical bonds, intermetallic compounds, and solid solutions, which enhance interfacial bonding. During crystallization and cooling, the metal at the interface forms a structure with higher hardness, strength, and wear resistance, resulting in a well-bonded interface that improves material properties. Interfacial bonding can be significantly enhanced by selecting suitable coating materials, optimizing the MAM process parameters, employing preheating and post-treatment techniques, adding intermediate layer materials, alloying, and employing heat treatment techniques.

3. Microscopic Effects of RECs in the MAM Process

REEs, with distinct physical and chemical properties, provide a wide range of favorable effects on the product's performance in the MAM. We have already mentioned how REEs can improve the cladding layer's molten pool fluidity, purity, and interfacial bond strength. This section will dive deeper into RECs' involvement in refining microstructure, homogenizing composition, and promoting columnar to equiaxed transition.

3.1. Mechanism of REEs on the Refinement of Microstructure

REEs have the effect of grain refinement; the grain sizes of AA2219 composites reinforced with 0, 0.5, 1.0, 1.5, and 2 wt.% CeO_2 are 483 µm, 453 µm, 411 µm, 362 µm, and 328 µm, respectively [56]. The incorporation of CeO_2 significantly reduces the dendritic morphology and refines the α-Al grain structure. However, excessive or slight amounts of REOs would lead to an increase in grain size and interstitial space, which negatively affects the density and hardness of the material. Yang et al. [57] demonstrated that appropriate

amounts of REOs can significantly refine precipitated Si. When the CeO_2 content is 0.6 wt.%, the average diameter of precipitated Si in the composites is the smallest. When the CeO_2 content is less than 0.6 wt.%, the average diameter decreases with the increase in CeO_2 content. When the CeO_2 content is greater than 0.6 wt.%, the average diameter increases with the increase in CeO_2 content. The mechanism of grain refinement by REEs is analyzed as follows:

3.1.1. Expansion of Nucleation Sites

At the small critical undercooling limit ΔT_n, REEs promote heterogeneous nucleation of the substrate material. Tan et al. [58] attributed the grain refinement to the superior crystallographic atom matching at the Al/LaB_6 interface, which has a low atomic mismatch. As demonstrated in Equation (2), ΔT_n is proportional to the lattice mismatch (δ). LaB_6 decreases the ΔT_n of Al heterogeneous nucleation and increases the rate of Al heterogeneous nucleation.

$$\Delta T_n = \frac{c_E}{\Delta S_v} \delta^2 \tag{2}$$

where c_E is the elasticity coefficient and ΔS_v is the entropy of phase transition per unit volume. When the temperature gradient ΔT exceeds ΔT_n of the equiaxed grains, the difficulty of nucleation between dendrites decreases, resulting in equiaxed grain nucleation and growth.

Uniformly distributed REEs can effectively function as heterogeneous cores, acting as "seeds" in the molten pool's solidification process, as shown at point B in Figure 7. REEs have a high melting point, which causes them to be partially dissolved and partially decomposed. Sun et al. [59] discovered that unmolten CeO_2 is the foundation of heterogeneous nucleation of (Ti, Nb)C/Ni and chromium carbides (Cr_7C_3 and $Cr_{23}C_6$). The nucleation sites in the coating increased as the CeO_2 addition increases while the size of (Ti, Nb)C/Ni gradually declined. When the CeO_2 addition reached 9 wt.%, the size of (Ti, Nb)C fell to 0.5 μm. Guo et al. [60] demonstrated that nano-Y_2O_3 increased the number of non-homogeneous nucleation sites in the α and γ phases, and the average grain sizes of T4822 and T486 alloys were lowered from 590 μm to 275 μm and 260 μm, respectively.
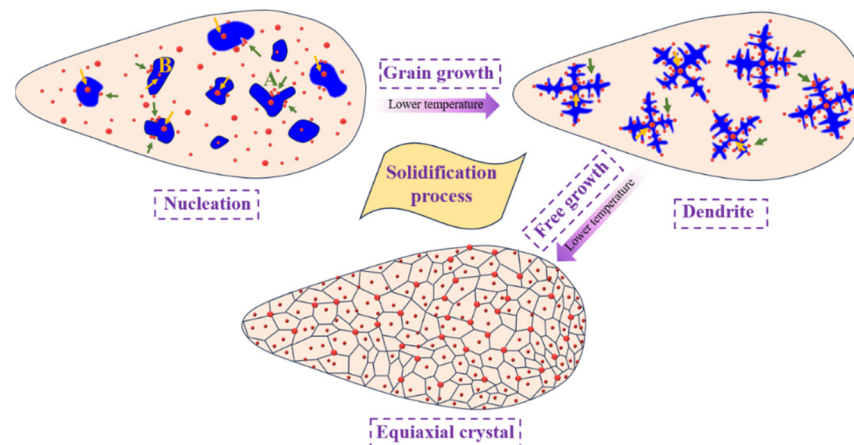

Figure 7. Effect of REEs on the solidification process of the molten pool.

According to existing research, the melting temperatures of nucleating agents are higher than that of the substrate. Melting points of CeO_2, La_2O_3, and Y_2O_3 are all over 2400 °C [61], whereas those of Al, Ti, and Fe substrate metals are around 660 °C, 1668 °C, and 1535 °C, respectively. When the molten pool reaches a specific temperature, the REOs begin to break down, and the RE-O chemical bond breaks. The broken REEs are reactive, forming intermetallic compounds, or REC/REN when they react with other elements. The undecomposed and generated high melting point RECs can operate as multiphase

nucleation sites, facilitating the nucleation of other substances in the molten pool and accelerating the material's solidification process.

3.1.2. Inhibition of Grain Growth

The enrichment of REEs in front of the solid–liquid boundary during solidification causes compositional subcooling, which slows solute diffusion and limits crystal growth rate. The magnitude of grain growth rate is generally evaluated by the growth inhibition factor Q, which is computed as:

$$Q = mC_0(k - 1) \tag{3}$$

where m is the slope of the liquid phase line in the binary phase diagram, C_0 is the concentration of the solute element, and k is the equilibrium partition coefficient of the solute element. Kang et al. [62] confirmed the discovery that Ce could alter the crystalline supercooling of AlSiMgFe alloys, increasing the Q value. Multiple REEs have a significantly stronger limiting influence than a single REE, and the actual Q of multiple REEs is greater than the total of each REE [63]. Jiang et al. [64,65] discovered that the atomic radius of La (0.1877 nm) was substantially bigger than that of Al (0.1180 nm), resulting in La atoms being essentially insoluble in the α-Al substrate. La was expelled and enriched in the GB, which limited the growth of α-Al grains. Small levels of REEs had minimal effect on the growth rate of α-Al grains, and 800 ppm La increased Q by 0.16K.

RECs remain stable during additive manufacturing heat cycling and accumulate at GB during solidification, performing a pinning theory on grain growth. This can effectively limit grain growth and improve material properties [66]. Gao et al. [67] discovered that Ce was concentrated at the GB of Ni-based coatings, resulting in resistance to GB growth. When the CeO_2 content was increased from 0 to 4.0 wt.%, the grain width fell from 1.74 μm to 237.5 nm. Zhang et al. [68] discovered that Y_2O_3 could be adsorbed at the primary β-Ti GB, reducing grain solid–liquid interface motion and inhibiting primary β-Ti grain growth. The Y_2O_3 pinning disrupts the GB continuity, resulting in the acicular martensite phase with typical penetrating crystal growth features. Except for directly adding RECs, compounds generated by REEs and metal elements have pinned on GB migration. Kang et al. [62] discovered that in AlSiMgFe alloys, Ce atoms interact with Al atoms to generate $Al_{11}Ce_3$ compounds, which inhibit GB migration. The average grain size of the 0.1Ce alloy was reduced by 47.6% compared to the substrate alloy. Therefore, directly added and indirectly generated RECs can refine grains and improve alloy properties during MAM solidification by preventing grain growth.

Many scholars have conducted a thorough investigation into the fundamental concept of REEs [69]. Due to the large radius and low solubility of REEs during solidification, REEs can be repelled into the GB via grain nucleation and development, as shown in Figure 8. The presence of more REEs in the grain interstitials hinders grains from touching each other, raising the Q-value and inhibiting its growth. If the amount of REEs in the interstices of the substrate grains is low, there will be a contact angle, expelling the REEs and accumulating in the contact neck. When the REEs accumulate in clusters, it restricts the expansion of the contact necks, ultimately creating a pinning effect.

In summary, REEs can improve the properties of materials by increasing the nucleation sites, inhibiting the growth of crystal grains, and reducing the critical undercooling in the process of microstructure refinement. The specific mechanism of action is as follows:

(1) The addition of REEs can increase the nucleation sites of the substrate material. During the cooling process of the molten pool, the undissolved REC and the generated high melting point RECs can be utilized as heterogeneous nucleation cores to promote the nucleation rate of the substrate alloys, which can refine the grains.

(2) REEs can inhibit grain growth. In the AM process, the addition of REEs can pin down grain growth and slow down the growth rate. This will refine the microstructure and improve the mechanical properties of the material.

(3) REEs also reduce the critical undercooling limit of the substrate materials. In the same cooling conditions, the existence of REEs can promote the crystallization of the material and increase the rate of nucleation, which can refine the grains.
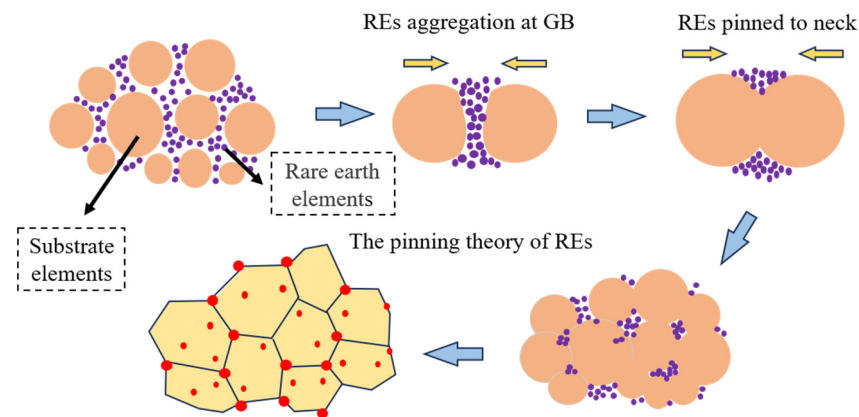

Figure 8. Mechanism of grain growth inhibition by REEs.

3.2. Mechanisms of REEs on Compositional Distribution

3.2.1. Distribution of REEs in Microstructure

Because the radii of REAs differ significantly from those of substrate atoms, REAs tend to dissolve and segregate at GB. The equilibrium grain boundary segregation concentration (C_{gb}) can be calculated using the equations developed by Mclean and Northcott based on statistical mechanics [70,71] as follows:

$$C_{gb} = \frac{C_m A exp(Q/RT)}{1 + C_m A exp(Q/RT)} \quad (4)$$

where C_m is the solubility of solute atoms in the crystal, A is the boundary vibrational entropy factor, Q is the distortion energy difference of solute atoms between the GB and the crystal, R is the gas constant, and T is the absolute temperature. As the solvent/solute radius difference increases, it leads to an increase in the distortion energy difference and C_{gb}. Wang et al. [72] observed that part of the La_2O_3 particles were decomposed into La atoms and entered the lattice during the preparation of La_2O_3-modified Fe-based composite coatings ($Fe_{78.5}Cr_{15.6}Ni_{4.0}Si_{0.7}$). Because the radius of La is 2.5 times that of Fe, the deformation energy of the composite coating containing La_2O_3 is greater than that of the composite coating without La_2O_3. As a result, REEs tend to dissolve and segregate along the GB, inhibiting alloy element diffusion in the molten pool. Molecular dynamics simulations [73] have demonstrated that polarizing elements with large ionic radii at GB or surfaces effectively reduce the energies. The greater the ionic radius, the lower the GB energy. REAs with large radii are prone to polarization at GB, which can significantly reduce GB energy and surface energy in the materials.

Significant segregation occurs during grain growth at the active sites of the GB, which means that the concentration of REEs at the crystal boundary is higher and the growth inhibitory factor of grains is large. Gao et al. [74] discovered that La elements gathered near the TiNi phase boundary, limiting grain growth, as shown in Figure 9a–d. The recombination reaction efficiency of Ti with Ni, C, and B elements is significantly increased, promoting molten pool flow and homogenizing the elements. Bian et al. [75] classified the Al substrate in Al-Fe-Ni-xSc alloys into three components labeled as: (1) incipient Al, (2) eutectic boundary Al (EPFA), and (3) eutectic interior Al. Sc is localized in the EPFA region as Al_3Sc, as shown in Figure 9e–g. In conclusion, the REEs are separated at GB because of the combination of characteristics such as atomic radii and chemical properties, which have a significant impact on the material's structure and properties. Li et al. [76] found that Ti, Al, and V were uniformly distributed in TC4 doped with and without Y_2O_3. However, the element Y is concentrated between the TC4 particles, as shown

in Figure 9h–j, and the EDS analysis showed that the distribution of the Y element is the same as the bright species.
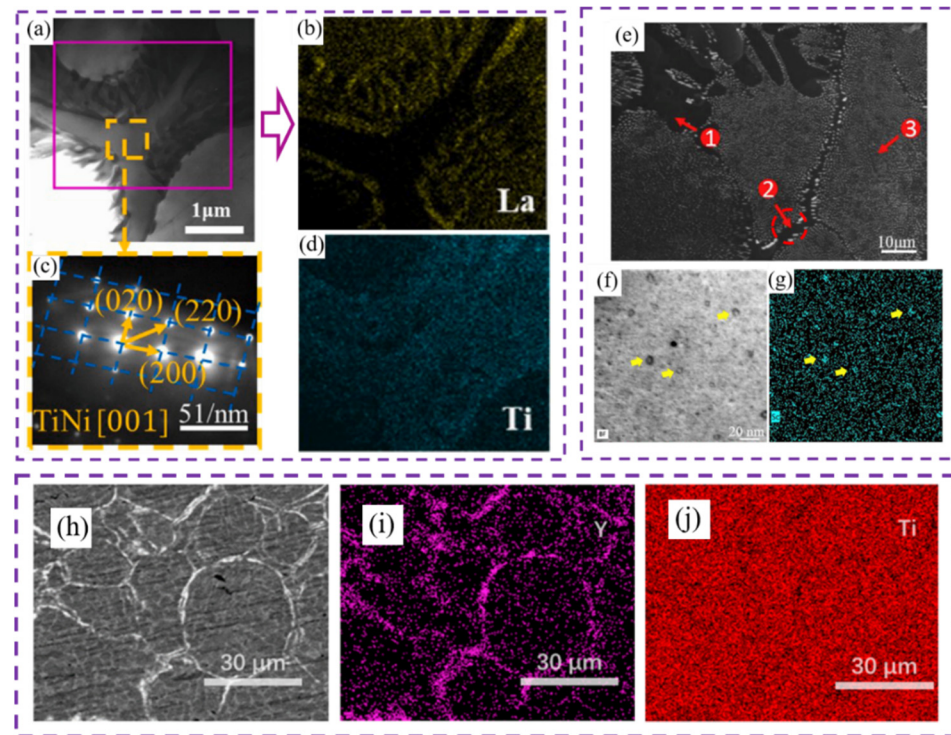

Figure 9. (**a**–**d**) The TEM-selected diffraction pattern and elemental surface scan map of the coating with the addition of 2.5 wt.% LaB$_6$ [74], (**e**–**g**) three Al-based sub-divisions of eutectic alloy and Sc element in EPFA [75], and (**h**–**j**) 2.0 wt.% Y$_2$O$_3$-TC4 sintered compact and elemental maps of Ti and Y [76]. Reprinted with permission from Ref. [74], 2023, ELSEVIER; Ref. [75], 2020, ELSEVIER; [76], 2018, ELSEVIER.

3.2.2. Distribution of Substrate Elements in Microstructure

REEs provide a stirring function in the molten pool, increasing fluidity and considerably facilitating the homogenous dispersion of diverse elements. Liang et al. [77] reported that the Ni60 alloy produced a poorly mobile molten pool devoid of REEs. The impurity Si failed to float out of the molten pool completely, and CeO$_2$ with a Si element concentration of around 4 wt.% enhanced flowability and stimulated the floating of elemental Si out of the molten pool with Si contents of less than 1%. REEs also improved the distribution of Cr and C, reducing variation from the surface to the bottom. Gao et al. [78] indicated weak mobility and diffusion of elements in the molten pool in Ni60 cladding layers without REEs, resulting in considerable aggregation and segregation. When the addition of La$_2$O$_3$ reached 1.6 wt.%, the elemental distribution was most homogeneous. The extra La$_2$O$_3$ reduced the mobility of the molten pool and enhanced microstructure inhomogeneity.

REEs accumulate at GB during the solidification process and are susceptible to chemical interactions with substrate elements, resulting in compound segregation. Zhang et al. [79] used laser cladding to explore the effect of Y$_2$O$_3$ on Ti-based composites and discovered that Y$_2$O$_3$ increases the aggregation of Cr elements at GB, generating secondary and tertiary dendrites. According to Li et al. [80], the microstructure of HEA coatings is composed of a white phase, gray phase, and black skeleton-like structure. Y$_2$O$_3$ has little effect on the phase transition but influences the production and distribution of the HCP and TiN phases. The gray phase is the BCC phase, which is high in Co, Ni, and Ti, whereas the white phase is high in Cr, Nb, and Ti. Through EDS research, He et al. [25] discovered that in CeO$_2$-modified FeCrNiMnAl alloys, tiny white dots were produced at GB, which consisted of Fe, Cr, Ni, Mn, Al, Ce, and O components. To avoid this segregated phenomenon, the addition and distribution of REEs must be reasonably regulated during

the material production process. In the La_2O_3/CoCrFeNiMoSi coatings [81], as shown in Figure 10a,b, La_2O_3 promotes the temperature gradient of the molten pool, crystal nucleation, and growth. Considerable secondary dendritic arms were produced, which broke the grain boundary structure and made the grain boundaries finer. From Figure 10c, it can be observed that the elements are uniformly distributed in the coating.
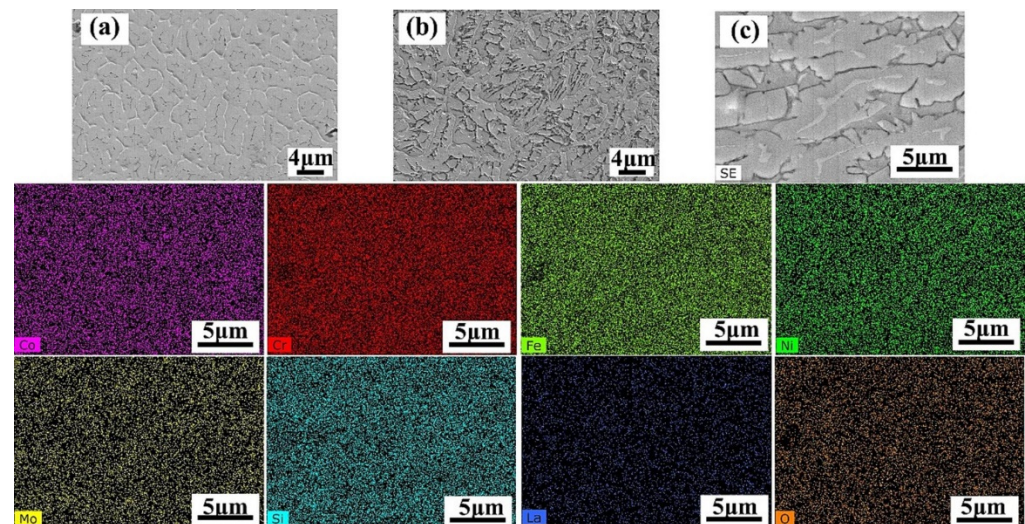

Figure 10. Microstructure of the coatings: (**a**) HEA, (**b**) La_2O_3/HEA, and (**c**) EDS of the La_2O_3/HEA [81]. Reprinted with permission from Ref. [81], 2024, ELSEVIER.

REEs can improve the surface tension, wettability, and chemical activity of the reinforced phase, resulting in improved dispersion and uniformity of distribution in the substrate. Wang et al. [82] discovered that the Ni, Al, and Cr elemental compositions of the coatings without REEs had a wide range of fluctuations and an extremely inhomogeneous distribution when REOs-modified Ni60 coatings were formed on the surface of 6063 aluminum alloy. The elemental distribution in CeO_2-, Y_2O_3-, and La_2O_3-modified coatings, on the other hand, was homogeneous, particularly in the 5% La_2O_3 coating. Yang et al. [83] used a laser beam to irradiate B_4C and Y_2O_3 hybrid powder, and the TiC phase in the composite coating was uniformly dispersed when the Y_2O_3 content was 0.5% to 1.5%. However, 2% of the Y on the TiC phase was inhomogeneously distributed, causing the Al_3Ti and TiC phases to cluster together and produce an inhomogeneous distribution. In conclusion, an appropriate amount of REEs is beneficial to the improvement of material structure and properties, but an excessive amount of REEs may cause clustering of substrate elements and jeopardize the material properties. Therefore, it is crucial to control the concentration and distribution of REEs.

REEs can improve the fluidity of the molten pool and promote the homogeneous distribution of substrate elements, which is beneficial to enhancing the comprehensive performance of coatings. However, the element distribution is a combined result of the element content, the molten pool environment, the atomic radius, and the chemical properties of the material. As a result, several investigations have found that REOs have a negligible influence on element dispersion and even impede the diffusion of substrate elements separated in the immediate area. To answer the issue of REEs altering element distribution, existing research has numerous disagreements and requires additional investigation.

3.3. Mechanisms of REE Effects on Grain Morphology

3.3.1. Modification of Grain Morphology

As illustrated in Section 2.2, RECs can separate, pin, and adsorb in the active sites at grain borders, lowering the system's Gibbs free energy and the driving force for grain growth. Xu et al. [84] discovered that cladding La_2O_3-modified Ni-based coatings on S136 steel resulted in the production of distinct morphologies of dendrites at different

portions of the dendritic arms at varied temperatures and solidification speeds. At lower La_2O_3 levels, element diffusion in the molten pool was faster, and the crystallization rate was slower, resulting in the creation of dendritic crystal formations. The diffusion of components in the molten pool slows down as the La_2O_3 concentration increases, the crystallization rate accelerates, and the dendritic shape eventually becomes elongated. When the concentration of La_2O_3 is higher, the crystallization rate is accelerated further, resulting in the restriction of element transport and the creation of a long dendritic structure.

During the solidification of grains in the molten pool, the fastest developing crystal surfaces have high surface tension and adsorption capability. REEs are the most active on these surfaces and are readily adsorbed, lowering the diffusion rate and changing the grain shape. The adsorption energy Γ^K of REEs on K crystal surfaces is calculated as [85]:

$$\Gamma^K = -\frac{C}{RT}\frac{d\gamma_C^K}{dC} \tag{5}$$

where C is the concentration of surface-active material in the molten pool, T is the absolute temperature, and γ_C^K is the surface tension of the crystalline surface K. Yang et al. [83] found that the Al_3Ti phase exists in the coating as rods and "X" shapes under normal conditions. Y_2O_3 adsorbs on the Al_3Ti phase, hindering the diffusion at the grain boundaries and altering the morphology of the Al_3Ti phase from rod-like to "X"-shaped. Zhang et al. [86] also discovered that CeO_2 has no effect on the compositional phase but influences the content of dendritic TiC_X, for example, 3 wt.% CeO_2 modified Ti-based coatings contain 35% dendritic TiC_X.

In the study of the influence of REE on the grain morphology of TiB_2 by employing first-principles calculations [87], it was found that TiB_2 nuclei grow synchronously in all directions in a spherical shape without REE doping, as shown in ① and ② in Figure 11. However, the surface energy gradually decreases as the nucleus grows, which results in crystalline surfaces with high refractive indices covering the surface and forming a polyhedral morphology, as shown in Figure 11 ③. The different surface tensions of these crystal surfaces result in different crystal growth rates, eventually forming hexagonal disk shapes surrounded by {0001} and {10-10} small planes, as shown in Figure 11 ④. The Sc can be preferentially adsorbed on the high-energy {10-11} and {11-20} surfaces during the formation of crystalline surfaces with high refractive indices, which restricts the growth rate of these surfaces and transforms the morphology of TiB_2 from hexagonal shape to spherical shape. REE adsorbed on the surface of faster growing crystals not only reduces the difference in surface energy of the crystals but also hinders the rapid growth of crystal surfaces with maximum surface tension, which improves the morphology of the grains.
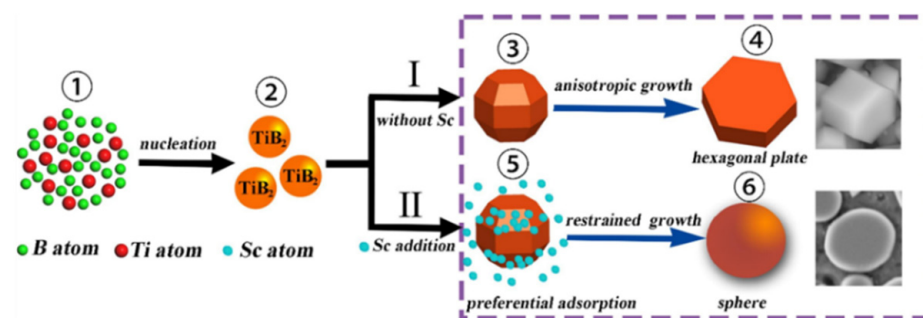

Figure 11. Mechanism of the contribution of the Sc to the grain morphology of TiB_2 [87]. Reprinted with permission from Ref. [87], 2020, ELSEVIER.

3.3.2. Promotion of Columnar to Equiaxed Transition

Since REE can transform the morphology of grains, it is utilized in the MAM to achieve the process of columnar to equiaxed transition (CET), which has been demonstrated in Al alloys [88], Ni alloys [26], and Ti alloys [89]. Tan et al. [90] found that when 0.2 wt.% LaB_6 was added in AlSi10Mg alloys, columnar grains were nearly eliminated, and 88%

of the equiaxed grains were distributed in the range of 0.5 μm–4.5 μm. More than 80% of the grains in the 2 wt.% LaB$_6$ modified alloys were ultrafine equiaxed grains below 2 μm. Bermingham et al. [91] concluded that La$_2$O$_3$ was a heterogeneous nucleation site for β-Ti, which refined the grain size by 85% and produced an equiaxed warp zone at the top of the cladding layer. However, columnar grains were produced at the bottom due to the epitaxial growth of the grains.

Most researchers have shown that the solidification process of alloys can be finely regulated by controlling the content and type of REE. REEs modify the nucleation and growth behavior of grains, resulting in alloys with specific morphology, structure, and properties. However, the research is also insufficient for RE in AM. If too little RE is added, the refining effect is not obvious; if too much is added, other adverse effects may occur. Therefore, there is an urgent need to study the quantitative relationship between the content of REE and the refinement effect.

3.4. Effect of REE in Laser Cladding

In summary, we analyze in detail the role of REEs in the powder mixing process, the laser-powder process, and the laser-powder-substrate process based on laser cladding. REEs improve powder flow and loose loading density during the powder mixing process, which aids in the formation of a uniform cladding layer.

In the laser-powder process, REEs have a specific energy level structure that absorbs laser energy at specific wavelengths. If the REEs in the hybrid powder match the wavelength of the laser, the REEs will absorb the laser energy preferentially. The particle size of commonly used REEs is on the micro- or nano-scale. REEs react with powder to alter particle size and morphology, increase surface area to volume ratio, and improve laser absorption. Increased laser absorption increases the local temperature of the mixed powder, which improves molten pool flow.

REEs act as refining agents in the laser-powder-substrate process, forming many fine nuclei in the molten pool, which promotes crystal growth and refines the grains. In terms of interfacial bond strength, REEs react with the elements in the substrate to form a metallurgical bonding interface with high bonding strength, improving the cladding layer's adhesion. In terms of interfacial bond strength, REEs react with the elements in the substrate to form a metallurgical bonding interface with high bonding strength, thus improving the adhesion of the cladding layer. REEs can also react with gases and impurities in the molten pool, reducing porosity and inclusions as well as purifying the molten pool.

REEs play an important role in the laser cladding process, optimizing the structure and properties of the cladding layer by improving the powder fluidity, absorbing the laser energy, refining the grain, removing impurities, and strengthening the interfacial bonding. Therefore, the rational utilization of REEs in laser cladding technology can obtain cladding layers with excellent properties, which provides a new way for industrial manufacturing and material surface modification.

4. Effect of REOs on the Improvement of Tribological Properties

We investigate how REEs affect the microstructure and compositional distribution of alloys, revealing REE's positive role in optimizing the material structure, which is closely related to tribological properties. Numerous studies indicate that REOs can remarkably improve the tribological properties of alloys. By refining the microstructure, homogenizing the distribution of components, and modifying the chemical composition and microstructure of the friction surfaces, REOs influence the friction surfaces' adhesion and wear behavior, thereby improving the tribological properties of alloys.

4.1. Effect of REO Content on Wear Resistance

REOs have large atomic radii, which can promote grain nucleation and grain refinement by heterogeneous nucleation. At the same time, REOs can also increase the amount of liquid phase to fill the interstices of the grains and improve the density and hardness of

the material. Zhang et al. [92] discovered that with the increase in Y_2O_3 content in Al-Si coatings, the grains gradually became finer and then coarser, and the surface hardness and wear resistance were also enhanced and then weakened. The coating with 7.5 wt.% Y_2O_3 had the finest grain, the highest density, and the best surface properties, with an average hardness of 285.0 HV that was 3.6 times that of the substrate and a wear amount of 0.4584 mm^3 that was 26.68% that of the substrate.

The appropriate amount of REE significantly improves the wear resistance of the material, making the wear mechanism change from complex to simple abrasive wear. In the Mg-1.5Zn-0.6Zr alloy [93], the Vickers hardness increased from 54 HV to 60 HV, and the COF decreased from 0.132 to 0.127 as the addition of Sc element increased to 1.0 wt.%. The flaking phenomenon of the wear process is gradually weakened with the addition of Sc elements, and the wear surface gradually becomes smooth. The delamination wear is weakened, and the wear mechanism is gradually dominated by abrasive wear. In the AA6082 alloy [94], the wear behavior depends on the volume percentage of Y_2O_3. As the volume fraction of Y_2O_3 increases to 9 vol.%, the hardness increases by 60%, the wear rate decreases by 48%, and the wear mechanism changes from adhesive wear to abrasive wear. It has been found that REE can transform the microstructure of metallic materials, leading to greater refinement and homogeneity. This improves the hardness and toughness of the material, reduces the wear rate of the material during wear and alters the wear behavior as shown in Table 1. At the same time, REE can also form a layer of dense oxide film on the metal surface, which notably enhances the anti-wear performance of the metal surface.

The addition of a small quantity of REEs does not yield the desired reinforcing effect, whereas an excessive amount may lead to adverse effects, as indicated in Table 1. Sharma et al. [101] performed pin-on-disk wear experiments on Al-based composites containing 2.5 wt.% CeO_2. The experiments were carried out with a velocity of 0.5 m/s and a normal load of 10 N. The results indicated that the inclusion of REEs led to a significant increase of 87.28% in the wear rate. Abrasive wear was the predominant mechanism. However, when the content of CeO_2 exceeded a certain threshold, the wear mechanism shifted to delamination wear, which resulted in a significant increase in the surface roughness of the material. On the surface of S420 steel, Wang et al. [102] used laser cladding to prepare CeO_2-modified Al-based composites and found that the wear mechanisms were mainly microcutting and oxidative wear without the addition of CeO_2, and abrasive, microcutting, and adhesive wear with the addition of 1.0%, 1.5%, and 2.0% CeO_2. It was also stated [103] that a small amount of Y_2O_3 can exhibit diffuse strengthening and ensure a relatively stable friction coefficient. However, excessive additions will weaken the interfacial bonding and lead to a reduction in the strength, plasticity, and toughness of the alloy.

The REOs must be rationally controlled during the AM process to determine the optimal amount of REOs to be added for the best wear resistance and other important performance indicators. However, wear performance is the combined effect of the wear environment, wear parameters, and material properties. At present, it is difficult to systematically elucidate the influence mechanism of REE content on the wear mechanism and the qualitative relationship between the REO content and its influence on the mechanical or tribological properties of the substrate materials through single-factor experiments.

Table 1. Effect of REC content on the tribological behavior of materials.

Substrate/Powders	RECs	Content	Wear Mode	Abrasive Material	Hardness	Wear Depth or COF	Wear Mechanism	Ref.
65Mn/Ni60a + SiC	La_2O_3	0 wt.% 1 wt.% 1.5 wt.% 2 wt.% 2.5 wt.%	Rotating friction mode	GCr15	870 HV 873 HV 916 HV 991 HV 1215 HV	19.21 μm 20.21 μm 19.67 μm 15.79 μm 23.46 μm	Abrasive and mechanical wear Fatigue wear and plastic deformation Abrasive and mechanical wear Slight peeling Fatigue wear and plastic deformation	[95]
PI + PAI + Ep-44 + PTFE + DMF + WS_2	CeO_2	1.5 wt.% 2 wt.% 2.5 wt.%	Reciprocating sliding friction wear	304	0.224 GPa 0.220 GPa 0.164 GPa	0.072 0.065 0.067	Abrasive wear and furrow Furrows and spalling pits Plough grooves and flaking pits	[96]
TC4/NiCr + Cr_3C_2	CeO_2	0 wt.% 1 wt.% 2 wt.% 3 wt.% 4 wt.%	Dry-sliding friction test	GCr15	488 $HV_{0.5}$ 472 $HV_{0.5}$ 464 $HV_{0.5}$ 487 $HV_{0.5}$ 472 $HV_{0.5}$	0.587 0.630 0.508 0.530 0.568	Furrow and adhesive deformation Abrasive wear Abrasive wear Abrasive wear Abrasive wear	[97]
AZ61D	La_2O_3	0.5 wt.% 1 wt.% 2 wt.%	Scratch test	Diamond	116 HV 120 HV 130 HV	14.4 μm 13.3 μm 13.0 μm	Elastic deformation Slight furrow	[98]
TC4/TiB + TiC	LaB_6	0.2 vol.% 0.4 vol.% 0.8 vol.%	Pins and discs	Cr12MoV	53.5 HRC 54.5 HRC 54.8 HRC	0.248 0.228 0.231	Slightly wear tracks Small scratches and furrows Wear tracks and more La_2O_3	[99]
ADC12/Al	Pr + Ce	0 wt.% 0.3 wt.% 0.6 wt.% 0.9 wt.%	Pin-on-disc	45[#] steel	80 HV 90 HV 110 HV 105 HV	0.378 0.362 0.349 0.358	Abrasive and surface fatigue wear Adhesive wear Abrasive wear Adhesive wear	[100]

4.2. Effect of REC Type on Wear Resistance

Different types of RECs have different chemical–physical properties. For example, the Ce element has strong catalytic activity and promotes the formation of an oxide film on the surface of the material [104]; Yb_2O_3 improves the wear resistance of the materials, but the effect of Tm_2O_3 is opposite [105]. Zhang et al. [106] found that Ce^{4+} was more likely than Sm^{3+} to adhere to GB. The dendritic morphology of the nickel-based alloys became finer and denser with the addition of REOs. The eutectic layer spacing of CeO_2-doped nickel-based specimens was smaller than that of Sm_2O_3 specimens (d_{CeO_2} = 0.3–0.5 μm; $d_{Sm_2O_3}$ = 0.7–1.0 μm). Under high-load (200 N) abrasion, the specimen surface of CeO_2 exhibits shallower cut grooves and stronger abrasion resistance than nano-Sm_2O_3. While studying the effect of different RECs on tribological properties, Su et al. [107] found that the average microhardness values of Y_2O_3-, YCl_3-, and YF_3-modified Ni-Ti coatings were 755.1 $HV_{0.3}$, 579.1 $HV_{0.3}$, and 390.4 $HV_{0.3}$, respectively. The Y_2O_3 coating has the highest microhardness with a COF of 0.321 and a weight loss of 2.6 mg, and the wear mechanism is adhesive wear. The YF_3 coating has the lowest microhardness with a COF of 0.252 and a weight loss of 4.3 mg, and the wear mechanism is abrasive wear.

Besides, the atomic radii of Ce, La, and Y are 182.4, 187.7, and 162 pm, respectively, which are larger than those of common metallic elements [108]. The incorporation of REEs induces lattice distortion in the material, which is also an important factor in improving wear resistance. Based on nano-indentation tests, Zhang et al. [109] showed that the hardness of Y-doped Fe-based coatings increased to 16.5 GPa and Young's modulus decreased to 337.4 GPa. In addition, the hardness of Ce-doped coatings was like the ones without rare-earth elements, but the Young's modulus decreased to 344.4 GPa. Cao et al. [110] prepared hybridized reinforced Cu-matrix composites of La, Ce, and Y by refining TiB_2 particles from 654 nm to 515 nm (Ce), 567 nm (Y), and 596 nm (La), respectively.

The effect of different types of RECs on tribology is shown in Table 2, where the wear mechanism is complex. In conclusion, the mechanisms and effects of different REC types on the tribological properties of materials need further research and exploration. Future research could include an in-depth exploration of the interaction mechanism between REEs and materials, optimization of the addition and distribution of RECs, and exploration of new types of RECs. These studies will help to further understand the effect of RECs on the tribological properties of materials and provide new ideas and methods for the development of more wear-resistant, corrosion-resistant, and other high-performance materials.

4.3. Effect of REOs Dimensions on Wear Resistance

Both micro- and nano-scale REOs are beneficial for improving the microstructure. However, compared with micro-REOs, nano-REOs have higher diffusion coefficients, making them more likely to diffuse in the molten pool, and the strengthening effect is more pronounced. For example, the average porosity of CeO_2 nano-doped coatings is 0.4% higher than the micrometer scale, the surface roughness is 7% lower, and the average microhardness is 36% higher [119]. In the microstructure, coatings with micro-CeO_2 grow oriented dendrites and coarse equiaxed dendrites, while coatings with nano-CeO_2 grow multioriented dendrites and finer equiaxed dendrites [120]. Both nano-scale and microscale REOs can improve the wear resistance of materials, but nano-REOs have more advantages.

The nano-REOs show better results in terms of wear behavior. Chauhan et al. [119] found that the wear mechanisms of micro-CeO_2 coatings are abrasive wear and fatigue wear, whereas the wear mechanisms of nano-CeO_2 coatings are abrasive wear, which means that the nano-CeO_2 coatings perform better in resisting abrasive wear. Weng et al. [121] revealed the REOs-modified materials would form cracks and expand on the wear surface at the micron scale, leading to severe spalling. In nano-REOs-modified alloys, a fine microstructure was formed in the composites. Compared with the micro-REOs materials, the cracks in the nano-REOs materials are drastically deflected, and fewer oxygen atoms enter the substrate. Crack generation and extension are restrained, the oxide layer becomes thinner, and the surface appears to be slightly spalling, as shown in Figure 12.

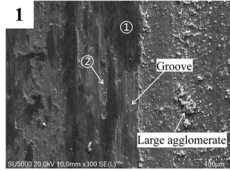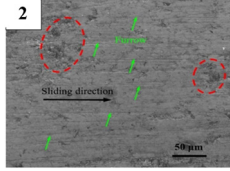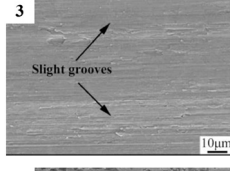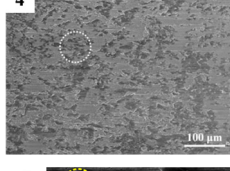Table 2. Effect of different RECs on the wear resistance of modified materials.
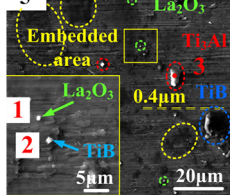
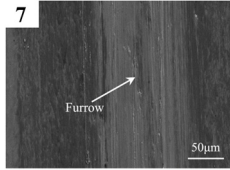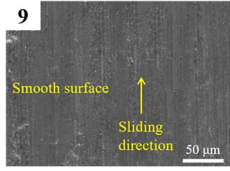| Substrate/Powders	REC	Processing	Content	Reinforced Phases	Surface Wear	Hardness	Wear Mechanism	Ref.
AZ91D/$Zr_{55}Cu_{30}Al_{10}Ni_5$	Nd_2O_3	Laser cladding	1.0 wt.%	$Al_5Ni_3Zr_2$, Zr_3O, $Nd_2Zr_2O_7$, $AlNdO_3$, and ZrO_2		689.8 $HV_{0.2}$	Abrasive wear formation, and eventual removal of the oxide layer	[18]
Low-carbon steel/WC	CeO_2	Laser cladding	2.0 wt.%	WC, W_2C, Ni_7W_3, and $Fe_{0.61}Ni_{0.32}$		525 HV_2	Microcutting wear and adhesive wear	[26]
Ti811/TC4 + Ni60	CeO_2 20–40 μm	Laser cladding	2.0 wt.%	TiC, Ti_2Ni, and TiB_2		846 $HV_{0.5}$	Adhesive wear, abrasive wear, and flat surface	[27]
TC4/Co42 + TiN	Y_2O_3 0.05–5 μm	Laser cladding	1.0 wt.%	γ-Co/Ni, TiN, CoTi, $CoTi_2$, NiTi, TiC, Cr_7C_3, TiB, Ti_5Si_3, and $aTi_{0.3}N_{0.7}$		1197.9 $HV_{0.2}$	Slight spalling	[36]
TC4/Ti + AlB_2	LaB_6	Laser cladding	3.0 wt.%	La_2O_3, Ti_3Al, and TiB		917 $HV_{0.5}$	Microcutting and brittle debonding	[40]

Table 2. *Cont.*
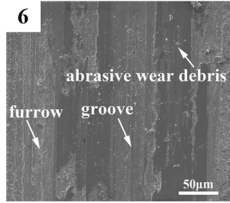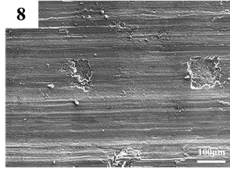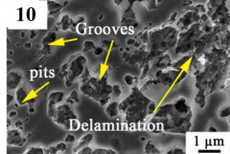
Substrate/Powders	REC	Processing	Content	Reinforced Phases	Surface Wear	Hardness	Wear Mechanism	Ref.
AISI 1045/Mo_2FeB_2 + Cr_3C_2 + W	La_2O_3 1–2 μm	Laser cladding	0.3 wt.%	Mo_2FeB_2, Fe_7Ni_3, Fe_3C, Cr_3C_2, CrB_2, FeNi, Cr_7C_3, WC, WC_{1-x}, and W_2C		1494.7 $HV_{0.5}$	Abrasive wear	[46]
45/Fe-based powder	La_2O_3 4 μm	Laser cladding	1.0 wt.%	Fe-Cr and Fe-Cr-Ni phases		523.76 $HV_{0.3}$	Slight abrasive wear	[72]
AZ91D/Al + Ti + B_4C	Y_2O_3	Laser cladding	1.5 wt.%	$AlTi_3(C, N)_{0.6}$, Al_3Ti, $MgAl_2O_4$, TiC, AlB_{12}, and $Al_{12}Mg_{17}$		398 HV	Abrasive wear and adhesive wear	[83]
Al6061/Ti + AlB_2	Sc_2O_3	Laser cladding	0.6 wt.%	TiB_2 and Al phases		920 HV	Microcutting	[87]
65Mn/Ni60A + SiC	La_2O_3 40 nm	Laser cladding	2 wt.%	Cr_7C_3, Cr_3Ni_2SiC, CrC, and Cr7C3		991 HV	Slight peeling	[95]

Table 2. *Cont.*
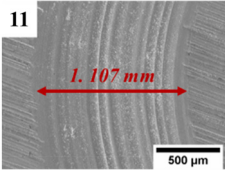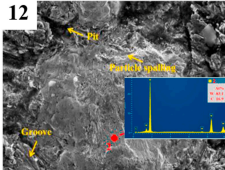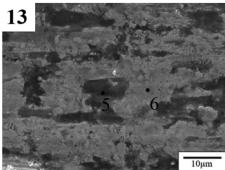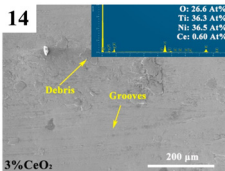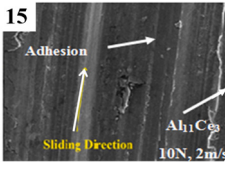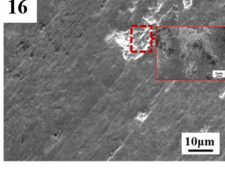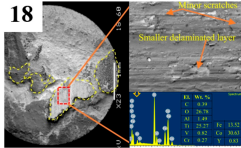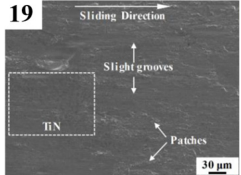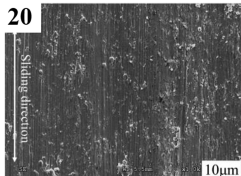
Substrate/Powders	REC	Processing	Content	Reinforced Phases	Surface Wear	Hardness	Wear Mechanism	Ref.
TC4/NiTi	YCl$_3$	Laser cladding	2.0 wt.%	NiTi and NiTi$_2$		579.1 HV$_{0.3}$	Abrasive wear	[107]
45/WC	Yttrium	Vacuum sintering	0.6 wt.%	Fe$_3$W$_3$C		16.50 GPa	WC particle spalling, cracks, and pits	[109]
TC4/TC4 + B$_4$C	LaB$_6$ 10–30 μm	Laser cladding	2.0 wt.%	TiC, TiB$_2$, and TiB		1243.4 HV$_{0.2}$	Abrasive wear, adhesive wear, and flat surface	[111]
NiTi	CeO$_2$ 50 nm	LPBF	3.0 wt.%	NiCe		380 HV	Adhesive wear, abrasive wear, and oxidative wear	[112]
Al6061/ SiC + Al$_2$O$_3$	CeO$_2$ 5 μm	Stir cast	2.5 wt.%	α-Al, Al$_{11}$Ce$_3$, Al$_4$Ce, Al$_3$Ce, and Al$_8$Mg$_5$		93.5 HVav	Abrasion, ploughing, and delamination	[113]
Cr$_3$C$_2$ + NiCr + CoCrMo	CeO$_2$ 20–50 nm	HVOF	4.0 wt.%	Cr$_2$O$_3$, Cr$_3$C$_2$, Cr$_{1.12}$Ni$_{2.88}$, NiCr$_2$O$_4$, and CoCr$_2$O$_4$		962.2 HV$_{0.5}$	Abrasive wear and surface fatigue wear	[114]

Table 2. *Cont.*

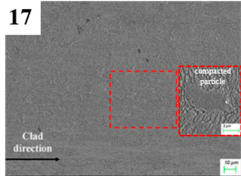| Substrate/Powders	REC	Processing	Content	Reinforced Phases	Surface Wear	Hardness	Wear Mechanism	Ref.
Q235/17Cr2NiSiMo	Y_2O_3	Plasma-clad	0.4 wt.%	Fe-Cr, α-Fe, and Y_2SiO_5		643.64 $HV_{0.1}$	Plastic deformation to slight peeling	[115]
TC4/TiC-Co	Y_2O_3 20–50 nm	TIG cladding	2.0 wt.%	$Al_2Ti_4C_2$, CoO, TiO_2, and Al_2O_3		1200 $HV_{0.05}$	Minor scratches and delaminated	[116]
TC4/h-BN	Y_2O_3	Laser cladding	1.0 wt.%	TiN, TiB, and α-Ti		891 $HV_{0.5}$	Abrasive wear and microcutting	[117]
TC4/Ni45 + Co-WC	Y_2O_3	Laser cladding	3.0 wt.%	TiB_2, TiC, Ti_2Ni, WC, and α-Ti		480 $HV_{0.5}$	Abrasive wear	[118]
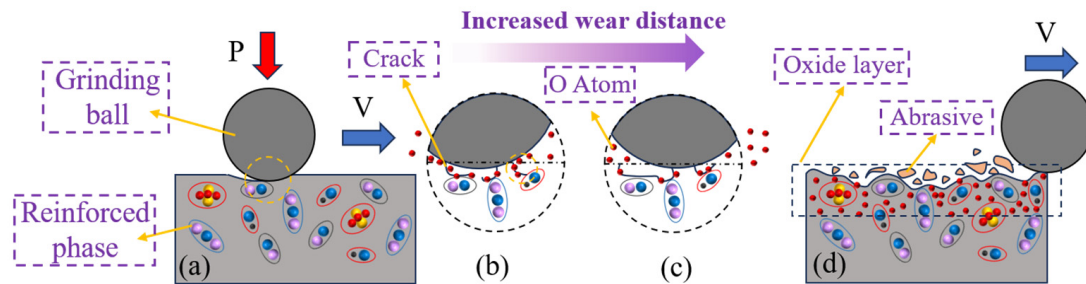
Figure 12. Effect of micro- and nano-REOs on wear behavior, including the beginning of wear (**a**), crack expansion (**b**), surface oxidation (**c**), as well as the end of wear (**d**).

Due to their high surface energy and activity, nano-REOs can form a more homogeneous interfacial structure with the base material to reduce cracks caused by stress concentration. Furthermore, nano-REOs can improve the wear resistance of materials by hindering dislocation motion and inhibiting plastic deformation. Micron-scale REOs can also improve the wear resistance of materials, but nano-scale REOs have more advantages in improving the wear resistance and wear behavior of materials.

4.4. Mechanisms of REOs on Tribological Properties

Due to the strong and hard character of REOs, it is helpful to directly strengthen the substrate and hinder dislocation movement, thereby increasing the material's hardness. For example, when 2 wt.% CeO_2 + La_2O_3 mixed powders were added to Al6063, the hardness of the material increased to 114.24 HV [122]. In addition to the inherent strong and hard properties, REOs also refine the microstructure [123], homogenize the tissue composition [124], and then improve the wear resistance of the material. Zhang et al. [124] discovered that the microstructure of Ti-based coatings gradually refined with the increase in Y_2O_3 content. The wear mechanism of the 3% Y_2O_3 coating was abrasive wear, and the wear volume and average COF were 113.82×10^3 mm^3 and 0.34, respectively, which were 47.8% and 10.5% lower than those of the coatings without REOs.

REOs with high chemical reactivity and unique electronic structures form reinforced phases with substrate elements and are uniformly distributed in the alloy, which significantly improves the hardness. For example, in Ti alloys [111,125,126], LaB_6 is decomposed into La and B atoms, which in situ generate TiB_X and La_2O_3 phases with Ti and O atoms, as shown in Figure 13. In NiTi alloys, Ce reacts with Ni atoms to produce a NiCe-modified composite. The depth/width ratio under different friction forces was reduced [112], and the COF in a 3.5% NaCl solution was reduced from 0.35 to 0.22 [127]. Bhoi et al. [128] added Y_2O_3 particles to Al-based composites, and the formed Al_3Y and Al_2O_3 reinforcements were uniformly dispersed in the substrate. Compared with specimens without Y_2O_3, the nano-hardness and elasticity modulus of the alloy with 5 wt.% Y_2O_3 increased by 143.6% and 80.55%, respectively. As shown in Tables 2 and 3, many studies have shown that REOs form high melting points and high hardness compounds with the substrate, which form uniformly distributed reinforced phases during solidification, significantly increasing the hardness of the alloys.

REOs change the crystal structure and grain boundary energy of alloys and control the phase transformation process, as shown in Table 3. Yi et al. [129] investigated the effect of Y on the microstructure of TiVAl alloys and found that the alloys are composed of the α' martensitic phase distributed along grain boundaries and the Y-rich phase. The Y-rich phase increases the martensitic phase transition temperature and weakens the transformation of the martensitic structure. Xu et al. [130] found that CeO_2 significantly affects the phase transition behavior of NiTi alloys, and the transition temperature of NiTi alloys increases first and then decreases with the increase in CeO_2 content. In CoCrFeNi alloys, Zhang et al. [131] found that the Y element transforms the face-centered cubic structure into a hexagonal structure and generates the $CaCu_5$ phase.

Table 3. Reinforced phases and hardness of REC-modified alloys.

| Substrate	Coatings	RECs	Contant	Reinforced Phases	Grain Morphology	Hardness	Ref.
AZ91D	Zr + Cu + Al + Ni	Nd_2O_3	1.5 wt.%	$Al_5Ni_3Zr_2$, Zr_3O, $Nd_2Zr_2O_7$, $AlNdO_3$, ZrO_2	Dendrites, cytocrysts, Nd-rich spherical structures, and amorphous substrate	689.8 $HV_{0.2}$	[18]
Ti811	TC4 and Ni60	CeO_2	2.0 wt.%	TiC, Ti_2Ni, TiB_2, α-Ti	Granular	790.4 $HV_{0.5}$	[27]
TC4	FeCoNiCrMo	LaB_6	2.0 wt.%	La_2O_3, TiBx, TiO_2, Fe_2O_3, Fe_3O_4, Cr_2O_3, MoO_2, MoO_3	Columnar and equiaxial crystals	987 $HV_{0.3}$	[125]
H13	Ni60	CeO_2	1.0 wt.%	γ-(Ni, Fe), TiC, Ni_2Si, $(Cr, Fe)_7C_3$, $Cr_{23}C_6$	Dendrites and equiaxed grains	900 $HV_{0.2}$	[132]
TC4	FeCoNiCrMo	CeO_2	2.0 wt.%	Fe-Cr, Al-Mo, Al-Ni	BCC	950 $HV_{0.3}$	[133]
42CrMo	Ni60 + WC	CeO_2	1.0 wt.%	Ni-Fe, W_2C, Fe_3C, $Cr_{23}C_6$, M_6C	Dendrites, cytocrysts, bars, and body crystals	560 $HV_{0.2}$	[134]
GCr15	Nope	La + Ce	0.003 wt.%	Fe_3N, Fe_4N	FCC, BCC	259.7 HV	[135]
Q235	Ni60 + WC	Y_2O_3	1.2 wt.%	WC, W_2C, $M_{23}C_6$, M_6C, Cr_7C_3, and other carbides	Dendrites and eutectic compounds	970 $HV_{0.5}$	[136]
AISI 304	TiB2 + Mo	Y_2O_3	1.0 wt.%	TiB_2, Ni_3Ti, Fe_3Mo, $MoNi_4$, NiTi, Mo_2B, Y_2TiO_7, Cr_2Ti, Fe_3B, Y_2O_3, and $MoNi_4$	Grain refinement	2170 $HV_{0.1}$	[137]
Q355B	316L + TiC	Y_2O_3	2.0 wt.%	Ni-Cr-Fe austenite phase	Cellular crystals	703.43 $HV_{0.2}$	[138]
AZ91D	TiC + Co	Y_2O_3	2.0 wt.%	TiC, Al_2O_3, Y_2C_3, Y_2Al, $TiCo_3$, and Co_2Ti	Granular	3374 $HV_{0.05}$	[139]
TC4	TiCN + SiO_2	CeO_2	3.0 wt.%	TiCN, TiN, Ti_6O, Ti_3SiC_2, and α-Ti phase	Smaller granular grains	1230 $HV_{0.2}$	[140]
5CrNiMo	Ti + Cr + Mo + B4C	Y_2O_3	3.0 wt.%	$(Ti,Mo)B_2$, $(Ti,Mo)C$, and $(Ti,Mo)C$	Rectangular-like, flower-like, and granular-like particles	1500 $HV_{0.2}$	[141]
Al6063	Al6063 + SiC	CeO_2 + La_2O_3	2.0 wt.%	Al_4Ce, Al_3Ce, Al_4La, and Al_8Mg_5	Grain size 28 ± 7 μm is refined to 14 ± 3 μm	114 ± 4.8 HV	[142]
TC4	Ni45 + NiCr-Cr_3C_2	CeO_2	2.0 wt.%	TiC, TiB_2, Ti_2Ni, and Ce_2O_3	Dendritic, long rod-shaped, micron-spherical, granular, and bulk-like phase	979 HV	[143]
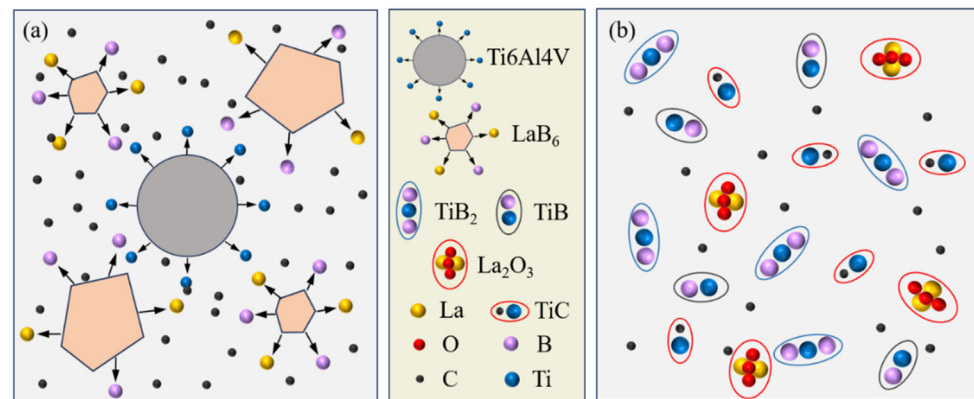
Figure 13. Mechanism diagram of LaB_6 promoting the generation of a reinforced phase from TC4 before (**a**) and after (**b**) reaction.

REOs can also enhance the hardness and wear resistance of the material by protecting the easily oxidized reinforced phase particles in the coating. For example, CeO_2 and La_2O_3 can effectively inhibit the decarburization and oxidation of WC during coating deposition [144,145], and the coating has the highest WC retention. The synergistic effect of WC and RE has a positive effect on improving the wear resistance of the coating through fine grain and phase strengthening (carbide). A small amount of REOs can increase the hardness of the coating to more than 1300 $HV_{0.5}$. In summary, except for intrinsically strong and hard properties, REOs can generate reinforced phases with high hardness, high thermal stability, and good chemical stability and promote uniform distribution of reinforced phases. REOs also control the phase transition process of the material and improve the mechanical properties of alloys.

5. Tribological Applications of REOs-Modified Materials

Coatings modified with REOs have a wide range of application prospects in the field of tribology, which can significantly improve the performance and life of the materials and bring important economic and social benefits to the fields of machinery manufacturing, automobile manufacturing, petrochemical industry, rail transportation, and marine engineering. With the continuous progress of science and technology and the expansion of application fields, the research of REEs is gradually deepened in the fields of extreme environment tribology and biotribology. In this section, the effects of REEs on high-temperature friction behavior and biological friction behavior are investigated.

5.1. Effect of REOs on High-Temperature Friction Behavior

In high-temperature tribology, REOs contribute to the reduction in the COF and wear rate by forming a film. For example, the engine components in the aerospace sector operate in high-temperature environments and need to have excellent resistance to high temperatures and friction [146]. The REOs in the modified materials can chemically react or physically adsorb at the friction interface to form a film with low shear strength, which can effectively mitigate the wear behavior.

REEs promote the formation of high-temperature-resistant reinforced phases in coatings. Du et al. [114] developed a novel Cr_3C_2-NiCrCoMo/nano-CeO_2 (NCE) coating based on the collaborative modification of the multielement alloy adhesive phase. It was found that the incorporation of CeO_2 lowered the threshold temperature for Ostwald ripening initiated by the secondary precipitated nano-Cr_3C_2 phase and promoted the growth and aggregation of Cr_3C_2 precipitated from the adherent phase of the NCE coating. The harnesses of the 4 wt.% CeO_2 coatings at 600 °C and 800 °C were 974.9 $HV_{0.5}$ and 992.0 $HV_{0.5}$, respectively, and the wear mechanisms were abrasive wear and surface fatigue wear. REEs can homogenize the reinforced phase distribution and increase the transition temperature of the wear mode. Yu et al. [147] found that CeO_2 improved the dispersion of TiB_2 and increased

the transition temperature of composites from mild to severe wear of TiB_2/A356 by 50 °C. The wear mechanism of the composites without CeO_2 at 90 N and 200 °C was metal flow and severe wear, while the CeO_2-doped composites were oxidized and delaminated wear.

In addition to the formation and uniform distribution of high-temperature-resistant reinforced phases, REEs can also form a dense oxide film on the surface. Han et al. [148] formed a black adhesion film consisting of C and O elements on the Fe-based coating under wear conditions at 350 °C and 100 N. The wear surface of the coating was smoothest when the CeO_2 content was 3%, and the wear mechanism was slightly abrasive and oxidative wear. In CeO_2-modified WC-12Co coatings [149], high temperatures promote the formation of new phases of WO_3 and CoO_4. The WO_3 phase would form a loose and unprotected structure, while the CoO_4 phase could form a dense oxide film. Therefore, the higher the ratio of CoO_4/WO_3, the higher the high-temperature wear resistance. CeO_2 promotes the uniform distribution of WC particles and obtains a high CoO_4/WO_3 ratio. Therefore, the CeO_2-modified WC-12Co coatings show a decrease in volume wear loss with increasing temperature, and the wear mechanism changes from microcutting wear to abrasive wear and oxidative wear.

In summary, CeO_2 is more widely used in high-temperature tribology. REOs can improve the wear resistance and high-temperature stability of materials by promoting the formation of high-temperature-resistant reinforced phases, uniform distribution, and the formation of a dense oxide film on the surface to safeguard mechanical operation in high-temperature environments. At present, the tribological properties and wear mechanisms of REE-modified coatings under different temperatures, speeds, and loads are indistinct, and the interactions and synergistic effects of other materials are unclear.

5.2. Effect of REOs on Biological Friction Behavior

In biotribology, coatings modified with REEs can be used to manufacture medical devices such as artificial joints and dental implants. These medical devices need to have excellent biocompatibility and wear resistance due to contact with human tissue. REEs can improve the biocompatibility of coatings and reduce the risk of inflammation and infection caused by implants, as well as improve wear resistance and reduce the wear and failure of implants. Among the biodegradable metals, Y_2O_3 enables the magnesium alloy coating to seal micropores, provide particle reinforcement, and enhance the adhesion of the coating to the substrate, with the degradation rate decreasing from 0.14 mm/a to 0.06 mm/a. Volume loss decreased from 0.46 mm^3 to 0.27 mm^3 for the same sliding distance, and the value of the grains' relative growth rate could be up to more than 90% [150]. REOs significantly improve the abrasion and degradation resistance of biodegradable coatings.

The effects of REE on the biotribological properties of additive manufacturing alloys are mainly reflected in improving the hardness, wear resistance, and biocompatibility of materials. In wear tests with Hank's solution, Tong et al. [151] found that β-type Ti alloys containing Sc showed lower COF and wear loss than those without Sc. The COF, wear loss, and hardness of the alloy without Sc addition were 1.283 ± 0.109 mg, 1.3 ± 0.1 mg, and 251 HV, respectively. The titanium alloy with Sc addition was 1.193 ± 0.112 mg, 1.0 ± 0.1 mg, and 265 HV, respectively. Moreover, Sc-doped titanium alloys showed no cytotoxicity and better cytocompatibility after incubation in an MG-63 cell culture medium for 3 days. Wang et al. [151] found that the TiCN + SiO_2 coating with CeO_2 addition significantly improved the wear resistance of the coating under SBF wear test conditions. The hardness of the coatings was 1230 $HV_{0.2}$, and wear volume loss was about 2.90% of the wear volume loss of the substrate. Because the fine microstructure of the coating improved fatigue wear resistance, the wear mechanism of CeO_2 coatings was abrasive and adhesive wear.

In addition to enhancing metal coatings, REEs also enhance the tribological properties of carbon films (DLC [152] and GLC [153,154]) and bone-like apatite. The dense structure of the DLC film results in excellent friction and wear resistance. The deformation of sp^3 bonds during the deposition of the DLC films results in the formation of residual

stresses, which severely weaken the bonding strength of the films to the substrate. The CeO_2 promotes an increase in sp^3-C content in the film. The DLC film at a cerium concentration of 1.16×10^3 mol/L is uniformly dense and has a maximum microhardness of 228.64 HV [155]. Liu et al. [156] found that the coatings doped with 0.2 wt.% La_2O_3 contained the maximum amount of HA and calcium phosphate. The La_2O_3-doped coating showed higher bone-like apatite precipitation after immersion in simulated body fluids compared to the La_2O_3-free coating. However, research on the application of REEs in biotribology is relatively limited, and further research and exploration of the potential applications and safety issues of REEs in biotribology are needed.

6. Conclusions

This paper summarizes the research progress of REEs on the tribological properties of MAM parts in recent years. The current research status of REEs in the fields of tissue modulation and surface tribology is described in detail in three aspects: microstructure, element distribution, and tribological properties. The main conclusions of this paper are as follows:

(1) The special electronic structure and lower surface energy of REEs can not only improve the laser absorption rate but also reduce the surface tension of the molten pool. The increased mobility of liquid metal in the molten pool makes it easier for the metal to fill into the mold or weld, thus reducing the generation of defects such as porosity and cracks.

(2) REEs can effectively purify the inclusions and metal impurities in the molten pool and improve the performance and quality of metal materials. This purification effect is mainly attributed to the REEs of denaturation, refinement, and interfacial tension reduction. In addition to improving the dilution of the molten pool, REEs also promote charge transfer and electronic interactions at the interface to form more stable chemical bonds. This improves the interfacial bond strength between the substrate and the coating.

(3) REEs have a variety of action mechanisms in the process of refining the microstructure, mainly by changing the solidification process and thermodynamic properties of the metal. Specific explanations for the role of REEs are: increasing the nucleation sites, inhibiting the growth of crystal grains, and reducing the critical degree of subcooling.

(4) In addition to intrinsic strong and hard properties, REEs can further enhance the properties of materials in several ways, including the protection of the reinforced phase particles, the formation of reinforced phases with substrate elements, the control of the phase transformation process, and the uniform distribution of the reinforced phases. These mechanisms help to improve the key performance indicators such as hardness, wear resistance, and corrosion resistance of the material.

(5) Moderate amounts of REEs can improve the hardness and wear resistance of metals, but too much or too little REEs may have negative effects. Compared with micro-REC particles, nano-RECs can obtain a finer and denser microstructure, and the prepared coatings have better hardness and wear resistance.

7. Perspective

According to the current research status of REEs in MAM, the existing problems and future development trends are presented from the aspects of microstructure regulation, structure into homogenized distribution, and tribological properties of modified materials. The perspective is as follows:

(1) The influence of REEs on the tribological properties of additively manufactured metals in different environments: The tribological properties of metal materials are affected by environmental factors such as temperature, humidity, and atmosphere. Research on the effect of REEs on the tribological properties of additive metals in different environments can help develop additive metal materials with excellent environmental adaptability.

(2)   Controllable preparation of REEs in additive manufacturing metals: In the process of additive manufacturing, factors such as the addition and distribution of REEs have an important impact on the properties of metal materials. The study of REEs in MAM can help to realize the effective regulation of properties.

(3)   Influence of REEs on the biocompatibility of additively manufactured metals: In some application scenarios, MAM alloys need to encounter biological tissues, such as in the biomedical field. Studying the effects of REEs on the biocompatibility of additively manufactured metals can help assess their potential for application in these fields.

(4)   The effects of REEs on molten pool fluidity and substrate element uniformity distribution are still controversial. On the one hand, REEs can lower the melting point, improve the fluidity of the molten pool, and promote the diffusion and homogeneous distribution of elements. On the other hand, the large atomic radius of REEs and the large differences in chemical properties with substrate elements lead to no significant effect of REEs on the homogeneous distribution of substrate elements and even inhibit the diffusion of substrate elements. Future research can focus on the interaction mechanism between REEs and substrate elements to investigate the diffusion behavior and distribution law in the molten pool.

Institutional Review Board Statement: Not applicable.

Informed Consent Statement: Not applicable.

Data Availability Statement: Data are contained within the article.

Conflicts of Interest: The authors declare that they have no known competing financial interests or personal relationships that could have appeared to influence the study reported in this paper.

References

1.   Gong, G.; Ye, J.; Chi, Y.; Zhao, Z.; Wang, Z.; Xia, G.; Du, X.; Tian, H.; Yu, H.; Chen, C. Research status of laser additive manufacturing for metal: A review. *J. Mater. Res. Technol.* **2021**, *15*, 855–884. [CrossRef]

2.   Blakey-Milner, B.; Gradl, P.; Snedden, G.; Brooks, M.; Pitot, J.; Lopez, E.; Leary, M.; Berto, F.; du Plessis, A. Metal additive manufacturing in aerospace: A review. *Mater. Des.* **2021**, *209*, 110008. [CrossRef]

3.   Kotadia, H.R.; Gibbons, G.; Das, A.; Howes, P.D. A review of laser powder bed fusion additive manufacturing of aluminium alloys: Microstructure and properties. *Addit. Manuf.* **2021**, *46*, 102155. [CrossRef]

4.   Kok, Y.; Tan, X.; Wang, P.; Nai, M.; Loh, N.; Liu, E.; Tor, S. Anisotropy and heterogeneity of microstructure and mechanical properties in metal additive manufacturing: A critical review. *Mater. Des.* **2018**, *139*, 565–586. [CrossRef]

5.   Wang, D.; Liu, L.; Deng, G.; Deng, C.; Bai, Y.; Yang, Y.; Wu, W.; Chen, J.; Liu, Y.; Wang, Y.; et al. Recent progress on additive manufacturing of multi-material structures with laser powder bed fusion. *Virtual Phys. Prototyp.* **2022**, *17*, 329–365. [CrossRef]

6.   Chadwick, A.F.; Voorhees, P.W. The development of grain structure during additive manufacturing. *Acta Mater.* **2021**, *211*, 116862. [CrossRef]

7.   Liu, Y.; Xiang, D.; Wang, K.; Yu, T. Corrosion of laser cladding high-entropy alloy coatings: A review. *Coatings* **2022**, *12*, 1669. [CrossRef]

8.   Xiang, D.D.; Wang, P.; Tan, X.P.; Chandra, S.; Wang, C.; Nai, M.L.S.; Tor, S.B.; Liu, W.Q.; Liu, E. Anisotropic microstructure and mechanical properties of additively manufactured Co-Cr-Mo alloy using selective electron beam melting for orthopedic implants. *Mater. Sci. Eng. A* **2019**, *765*, 138270. [CrossRef]

9.   Wang, Q.; Wu, G.; Tong, X. An investigation into wire arc additive manufacturing of Mg-Y-RE-Zr alloy. *Mater. Lett.* **2022**, *326*, 132922. [CrossRef]

10.   Hao, Z.; Qiu, Y.; Fan, Y.; Fu, W. Theoretical calculation and analysis of new rare earth cemented carbide based on first-principles. *Int. J. Refract. Met. Hard Mater.* **2021**, *101*, 105688. [CrossRef]

11.   Yin, X.; Liang, J.; Gao, Y.; Lin, Z.; Chen, S.; Liu, C.; Tian, K.; Zhang, H.; Tang, G. Effects of LaB_6 on the high-temperature oxidation behavior of $TiC+TiB_x$ reinforced titanium matrix composite coatings fabricated by laser cladding. *Surf. Coat. Technol.* **2021**, *421*, 127445. [CrossRef]

12. Stratiotou Efstratiadis, V.; Michailidis, N. Sustainable Recovery, Recycle of critical metals and rare earth elements from waste electric and electronic equipment (circuits, solar, wind) and their reusability in additive manufacturing applications: A review. *Metals* **2022**, *12*, 794. [CrossRef]

13. Artiushenko, O.; da Silva, R.F.; Zaitsev, V. Recent advances in functional materials for rare earth recovery: A review. *Sustain. Mater. Technol.* **2023**, *37*, e681. [CrossRef]

14. Hossain, M.K.; Raihan, G.A.; Akbar, M.A.; Kabir Rubel, M.H.; Ahmed, M.H.; Khan, M.I.; Hossain, S.; Sen, S.K.; Jalal, M.I.E.; El-Denglawey, A. Current applications and future potential of rare earth oxides in sustainable nuclear, radiation, and energy devices: A review. *ACS Appl. Electron. Mater.* **2022**, *4*, 3327–3353. [CrossRef]

15. Laha, S.S.; Thorat, N.D.; Singh, G.; Sathish, C.I.; Yi, J.; Dixit, A.; Vinu, A. Rare-earth doped iron oxide nanostructures for cancer theranostics: Magnetic hyperthermia and magnetic resonance imaging. *Small* **2022**, *18*, 2104855. [CrossRef] [PubMed]

16. Quezada-Novoa, V.; Titi, H.M.; Sarjeant, A.A.; Howarth, A.J. Building a shp: A rare-earth metal-organic framework and its application in a catalytic photooxidation reaction. *Chem. Mater.* **2021**, *33*, 4163–4169. [CrossRef]

17. Zhao, Z.; Wang, L.; Zhan, G.; Liu, Z.; Bian, Z.; Huang, C. Efficient rare earth cerium (III) complex with nanosecond d−f emission for blue organic light-emitting diodes. *Natl. Sci. Rev.* **2021**, *8*, nwaa193. [CrossRef]

18. Zhang, Y.; Guo, J.; Xu, G.; Li, Z.; Wei, S. Effect of Nd_2O_3 on microstructure, corrosion and wear properties of laser cladding Zr-based amorphous composite coatings on AZ91D magnesium alloy. *Appl. Surf. Sci.* **2023**, *611*, 155587. [CrossRef]

19. Liu, W.J.; Zeng, D.B.; Huang, H.S. Influence of rare-earth metal oxide coating on the structure and properties of laser strengthened area of cast iron. *Chin. J. Lasers* **1992**, *8*, 613.

20. Yang, Z.-Z.; Hao, H.; Gao, Q.; Cao, Y.-B.; Han, R.-H.; Qi, H.-B. Strengthening mechanism and high-temperature properties of H13 + WC/Y_2O_3 laser-cladding coatings. *Surf. Coat. Technol.* **2021**, *405*, 126544. [CrossRef]

21. Yang, L.; Yang, X.; Zhang, T.; Sun, R. Optimization of microstructure and properties of composite coatings by laser cladding on titanium alloy. *Ceram. Int.* **2021**, *47*, 2230–2243.

22. Hao, J.; Zhang, K.; Ren, P.; Chen, J.; Wang, M.; Zhang, Y.; Wen, M. Tuning the wettability, mechanical and tribological properties of NbN films by doping rare earth cerium. *J. Alloys Compd.* **2020**, *814*, 152339. [CrossRef]

23. Du, M.; Wang, L.; Gao, Z.; Yang, X.; Liu, T.; Zhan, X. Microstructure and element distribution characteristics of Y_2O_3 modulated WC reinforced coating on Invar alloys by laser cladding. *Opt. Laser Technol.* **2022**, *153*, 108205. [CrossRef]

24. Liu, L.; Wang, G.; Ren, K.; Di, Y.; Wang, L.; Rong, Y.; Wang, H. Marangoni flow patterns of molten pools in multi-pass laser cladding with added nano-CeO_2. *Addit. Manuf.* **2022**, *59*, 103156. [CrossRef]

25. He, R.; Wu, M.; Jie, D.; Cui, C.; Ou, B.; Miao, X.; Gong, Y. A novel approach to regulate the microstructure of laser-clad FeCrNiMnAl high entropy alloy via CeO_2 nanoparticles. *Surf. Coat. Technol.* **2023**, *473*, 130026. [CrossRef]

26. Shu, D.; Dai, S.; Wang, G.; Si, W.; Xiao, P.; Cui, X.; Chen, X. Influence of CeO_2 content on WC morphology and mechanical properties of WC/Ni matrix composites coating prepared by laser in-situ synthesis method. *J. Mater. Res. Technol.* **2020**, *9*, 11111–11120. [CrossRef]

27. Liu, Y.; Sun, R.; Niu, W.; Zhang, T.; Lei, W. Effects of CeO_2 on microstructure and properties of TiC/Ti_2Ni reinforced Ti-based laser cladding composite coatings. *Opt. Lasers Eng.* **2019**, *120*, 84–94.

28. Mahmoud, M.; Mosleh, A.O.; Mohamed, M.S.; El-Moayed, M.H.; Khalifa, W.; Pozdniakov, A.V.; Salem, S. The impact of Ce-containing precipitates on the solidification behavior, microstructure, and mechanical properties of Al-6063. *J. Alloys Compd.* **2023**, *948*, 169805. [CrossRef]

29. Li, D.; Cai, S.; Gu, J.; Liu, S.; Si, J. Co-doping of La/Ce and La/Er induced precipitation strengthening for designing high strength Al-Mg-Si electrical conductive alloys. *Mater. Today Commun.* **2023**, *36*, 106666. [CrossRef]

30. Ding, W.; Zhao, X.; Chen, T.; Zhang, H.; Liu, X.; Cheng, Y.; Lei, D. Effect of rare earth Y and Al-Ti-B master alloy on the microstructure and mechanical properties of 6063 aluminum alloy. *J. Alloys Compd.* **2020**, *830*, 154685. [CrossRef]

31. Tian, J.; Zhang, D.; Chen, Y.; Zhang, G.; Sun, J. Effect of nano Y_2O_3 addition on microstructure and room temperature tensile properties of Ti-48Al-2Cr-2Nb alloy. *Vacuum* **2019**, *170*, 108779. [CrossRef]

32. Zhong, H.; Li, S.; Zhang, Z.; Li, D.; Deng, H.; Chen, J.; Qi, L.; Ojo, O.A. Precipitation behavior, mechanical properties, and corrosion resistance of rare earth-modified Al-Zn-Mg-Cu alloys. *Mater. Today Commun.* **2022**, *31*, 103732. [CrossRef]

33. Yang, C.; Luan, Y.; Li, D.; Li, Y. Effects of rare earth elements on inclusions and impact toughness of high-carbon chromium bearing steel. *J. Mater. Sci. Technol.* **2019**, *35*, 1298–1308. [CrossRef]

34. Yin, B.; Hu, X.; Lu, Z.; Chou, K. The effect of Ce addition on purification and inclusion modification of CoCrFeNiMn high entropy alloy. *J. Alloys Compd.* **2023**, *934*, 167716. [CrossRef]

35. Chen, L.; Zhao, Y.; Guan, C.; Yu, T. Effects of CeO_2 addition on microstructure and properties of ceramics reinforced Fe-based coatings by laser cladding. *Int. J. Adv. Manuf. Technol.* **2021**, *115*, 2581–2593. [CrossRef]

36. Weng, F.; Yu, H.; Chen, C.; Liu, J.; Zhao, L. Microstructures and properties of TiN reinforced Co-based composite coatings modified with Y_2O_3 by laser cladding on Ti-6Al-4V alloy. *J. Alloys Compd.* **2015**, *650*, 178–184. [CrossRef]

37. Fang, Y.; Jin, K.; Liu, C.; Wang, H.; Wei, X.; Ding, Q.; Bei, H.; Zhao, X.; Zhang, Z. Effect of LaB_6 on the microstructure evolution and mechanical properties of Ti-45Al-8Nb alloy. *J. Alloys Compd.* **2023**, *938*, 168513. [CrossRef]

38. He, D.; Wang, H.; Huang, W.; Chen, X.; Lian, G.; Wang, Y. Microstructure and mechanical properties of LaB_6/Ti-6Al-4V composites fabricated by selective laser melting. *Metals* **2023**, *13*, 264. [CrossRef]

39. Liu, H.; Fu, P.; Liu, H.; Cao, Y.; Sun, C.; Du, N.; Li, D. Effects of rare earth elements on microstructure evolution and mechanical properties of 718H pre-hardened mold steel. *J. Mater. Sci. Technol.* **2020**, *50*, 245–256. [CrossRef]

40. Feng, Y.; Feng, K.; Yao, C.; Li, Z. Effect of LaB$_6$ addition on the microstructure and properties of (Ti$_3$Al + TiB)/Ti composites by laser cladding. *Mater. Des.* **2019**, *181*, 107959. [CrossRef]

41. Zhang, M.; Wang, X.H.; Qu, K.L.; Liu, S.S. Effect of rare earth oxide on microstructure and high temperature oxidation properties of laser cladding coatings on 5CrNiMo die steel substrate. *Opt. Laser Technol.* **2019**, *119*, 105597. [CrossRef]

42. Xiang, D.; Liu, Y.; Yu, T.; Wang, D.; Leng, X.; Wang, K.; Liu, L.; Pan, J.; Yao, S.; Chen, Z. Review on wear resistance of laser cladding high-entropy alloy coatings. *J. Mater. Res. Technol.* **2024**, *28*, 911–934. [CrossRef]

43. Cui, C.; Wu, M.; He, R.; Gong, Y.; Miao, X. Effect of CeO$_2$ addition on grain refinement and mechanical properties of Stellite-6 coating fabricated by laser cladding. *J. Therm. Spray Technol.* **2022**, *31*, 2621–2634. [CrossRef]

44. Chen, Y.; Chao, Y.J.; Luo, Z.; Cai, Y.; Ma, C. Microstructure and wear resistance of Co-based/Cr$_3$C$_2$ coatings with CeO$_2$. *Surf. Eng.* **2018**, *34*, 588–595. [CrossRef]

45. Zhang, P.; Mao, F.; Wang, Y.; Chen, C.; Xiong, M.; Wei, S.; Jiang, T.; Wang, C.; Zhang, C.; Wang, Z. Effect of rare-earth Sc on the interface microstructure and mechanical properties of Al/steel bimetallic composites prepared by liquid-solid casting. *J. Mater. Res. Technol.* **2023**, *24*, 808–823. [CrossRef]

46. Zhang, H.; Pan, Y.; Zhang, Y.; Lian, G.; Cao, Q.; Que, L. Microstructure, toughness, and tribological properties of laser cladded Mo$_2$FeB$_2$-based composite coating with in situ synthesized WC and La$_2$O$_3$ addition. *Surf. Coat. Technol.* **2022**, *449*, 128947. [CrossRef]

47. Zhang, J.; Li, X.; Xu, Q.; Hu, Y.; Guo, F.; Zhang, M.; Zhou, X.; Mao, C.; Tong, Y.; Peng, P. Effects of Ce and La elements on interfacial bonding, thermal damage and mechanical performance of brazed diamonds with Ni-Cr filler alloy. *Int. J. Refract. Met. Hard Mater.* **2021**, *98*, 105571. [CrossRef]

48. Wang, N.; Jin, T.; Sun, H.; Zhong, S.; Wen, G.; Yan, Z.; Xu, D. Exploring the trace rare earth Sm on the microstructure and mechanical performance of brazed diamonds by Ni-Cr filler alloy. *J. Mater. Res. Technol.* **2023**, *26*, 315–327. [CrossRef]

49. Wang, K.; Hu, S.; Zhong, Y.; Jin, S.; Zhou, Z.; Wang, Z.; Chen, J.; Wan, B.; Li, W. Effects of trace ytterbium addition on microstructure, mechanical and thermal properties of hypoeutectic Al-5Ni alloy. *J. Rare Earths* **2022**, *40*, 1305–1315. [CrossRef]

50. Jiang, N.; Lyu, H.; Li, Y.; Xu, N.; Zhang, H.; Zhou, N.; Zou, X.; Zhang, D. Enhanced interfacial adhesion of CF/PEEK-titanium hybrid laminates via rare-earth coordination interaction. *Compos. Sci. Technol.* **2023**, *239*, 110070. [CrossRef]

51. Zhang, X.; Yue, Y.; Xu, D.; Qin, J.; Zhang, X.; Liu, R. Effect of rare-earth elements on the interface of WC/α-Fe cemented carbide: A first-principles calculation. *Comput. Mater. Sci.* **2023**, *230*, 112483. [CrossRef]

52. Li, Z.; Lv, Q.; Wei, H.; Zhou, M.; Zhang, F.; Shan, Q. Effects of RE (Nd, Ce, Y, La) on TiC(100)/Fe(110) interface based on first-principles calculations. *Vacuum* **2022**, *205*, 111449. [CrossRef]

53. Shi, R.; Qian, S.; Zhao, D.; Shi, C.; He, C.; Sha, J.; Liu, E.; Zhao, N. Interface bonding and mechanical properties of copper/graphene interface doped with rare earth elements: First principles calculations. *Phys. E Low-Dimens. Syst. Nanostruct.* **2022**, *142*, 115260. [CrossRef]

54. Yan, M.; Wei, H.; Shi, X.; Jiang, Y. The influence of rare earth elements (Y, Sc) on the interfacial binding properties between the precipitation phases Fe$_2$B, FeB and the matrix Fe in boron steel. *Vacuum* **2023**, *215*, 112287. [CrossRef]

55. Aghajani, H.; Valefi, Z.; Zamani, P. Phase composition, microstructure, mechanical properties, and wear performance of nanostructured Al$_2$O$_3$ and Al$_2$O$_3$-Y$_2$O$_3$ coatings deposited by plasma spraying. *Appl. Surf. Sci.* **2022**, *585*, 152754. [CrossRef]

56. Karthik, A.; Srinivasan, S.A.; Karunanithi, R.; Babu, S.K.; Jain, V.K.S. Influence of CeO$_2$ reinforcement on microstructure, mechanical and wear behaviour of AA2219 squeeze cast composites. *J. Mater. Res. Technol.* **2021**, *14*, 797–807. [CrossRef]

57. Yang, B.; Wang, A.; Liu, K.; Liu, C.; Xie, J.; Wang, G.; Wei, S. Effects of CeO$_2$ content on friction and wear properties of SiCp/Al-Si composite prepared by powder metallurgy. *Materials* **2020**, *13*, 4547. [CrossRef]

58. Tan, Q.; Zhang, J.; Mo, N.; Fan, Z.; Yin, Y.; Bermingham, M.; Liu, Y.; Huang, H.; Zhang, M.-X. A novel method to 3D-print fine-grained AlSi10Mg alloy with isotropic properties via inoculation with LaB6 nanoparticles. *Addit. Manuf.* **2020**, *32*, 101034. [CrossRef]

59. Sun, S.; Fu, H.; Ping, X.; Guo, X.; Lin, J.; Lei, Y.; Wu, W.; Zhou, J. Effect of CeO$_2$ addition on microstructure and mechanical properties of in-situ (Ti, Nb)C/Ni coating. *Surf. Coat. Technol.* **2019**, *359*, 300–313. [CrossRef]

60. Guo, Y.; Chen, Y.; Xiao, S.; Tian, J.; Zheng, Z.; Xu, L. Influence of nano-Y$_2$O$_3$ addition on microstructure and tensile properties of high-Al TiAl alloys. *Mater. Sci. Eng. A* **2020**, *794*, 139803. [CrossRef]

61. Zhang, L.; Zhang, M.; Zhu, Z.; Gao, M.; Gao, J.; Guo, Z. Effects of nano-CeO$_2$ on microstructure and properties of Ni625 alloy prepared by laser cladding. *J. Alloys Compd.* **2022**, *918*, 165571. [CrossRef]

62. Kang, J.; Su, R.; Wu, D.; Liu, C.; Li, T.; Wang, L.; Narayanaswamy, B. Synergistic effects of Ce and Mg on the microstructure and tensile properties of Al-7Si-0.3Mg-0.2Fe alloy. *J. Alloys Compd.* **2019**, *796*, 267–278. [CrossRef]

63. Liu, X.; Yao, J.; Ma, X.; Wang, Y.S.; Gao, N.; Shi, Y.; Fan, Z.T.; Du, H. Columnar-to-equiaxed transition and grain refinement by solute interaction effects. *Mater. Charact.* **2023**, *205*, 113288. [CrossRef]

64. Jiang, H.; Zheng, Q.; Song, Y.; Li, Y.; Li, S.; He, J.; Zhang, L.; Zhao, J. Influence of minor La addition on the solidification, aging behaviors and the tensile properties of Al-Mg-Si alloys. *Mater. Charact.* **2022**, *185*, 111750. [CrossRef]

65. Jiang, H.; Li, S.; Zheng, Q.; Zhang, L.; He, J.; Song, Y.; Deng, C.; Zhao, J. Effect of minor lanthanum on the microstructures, tensile and electrical properties of Al-Fe alloys. *Mater. Des.* **2020**, *195*, 108991. [CrossRef]

66. Liu, L.; Qiao, Y.; Xu, P. Effect of La$_2$O$_3$ on microstructure and properties of laser cladding SMA coating on AISI 304 stainless steel. *Coatings* **2022**, *12*, 1004. [CrossRef]

67. Gao, Z.; Ren, H.; Geng, H.; Yu, Y.; Gao, Z.; Zhang, C. Effect of CeO$_2$ on microstructure and wear property of laser cladding Ni-based coatings fabricated on 35CrMoV steel. *J. Mater. Eng. Perform.* **2022**, *31*, 9534–9543. [CrossRef]

68. Zhang, T.; Xiao, H.; Zhang, Z.; Yao, B.; Yang, F. Effect of Y$_2$O$_3$ addition on microstructural characteristics and microhardness of laser-cladded Ti-6Al-4V alloy coating. *J. Mater. Eng. Perform.* **2020**, *29*, 8221–8235. [CrossRef]

69. Hu, T.; Shi, Z.; Shao, W.; Xing, X.; Zhou, Y.; Yang, Q. Effect of CeO$_2$ on density and wear resistance of Ni-Cr-WC coatings by theoretical calculation and experimental investigation. *Surf. Coat. Technol.* **2019**, *377*, 124850. [CrossRef]

70. Fang, Y.; Cui, X.; Cai, Z.; Wang, C.; Jin, G. Influence of La$_2$O$_3$ addition on nano indentation hardness and residual stress of Stellite 6 coating prepared by plasma cladding. *J. Rare Earths* **2018**, *36*, 873–878. [CrossRef]

71. Mclean, D.; Maradudin, A. Grain boundaries in metals. *Phys. Today* **1958**, *11*, 35–36. [CrossRef]

72. Wang, Q.; Yang, J.; Niu, W.; Li, Y.; Mao, X.; Wang, Y.; Zhang, K. Effect of La$_2$O$_3$ on microstructure and properties of Fe-based alloy coatings by laser cladding. *Optik* **2021**, *245*, 167653. [CrossRef]

73. Yi, H.; Che, J.; Liang, G.; Liu, X. Effect of rare earth elements on stability and sintering resistance of tetragonal zirconia for advanced thermal barrier coatings. *Crystals* **2021**, *11*, 287. [CrossRef]

74. Gao, Z.; Ke, L.; Li, J.; Qiao, Z.; Yuan, L.; Gao, Z.; Zhang, C. Effect of LaB$_6$ addition on the in-situ synthesis of TiB/Ti Ni/TiC reinforced Ni-based composite coatings. *Ceram. Int.* **2023**, *49*, 37454–37463. [CrossRef]

75. Bian, Z.; Xiao, Y.; Hu, L.; Liu, Y.; Chen, Z.; Wang, M.; Chen, D.; Wang, H. Stimulated heterogeneous distribution of Sc element and its correlated local hardening effect in Al-Fe-Ni-Sc alloy. *Mater. Sci. Eng. A* **2020**, *771*, 138650. [CrossRef]

76. Li, A.; Ma, S.; Yang, Y.; Zhou, S.; Shi, L.; Liu, M. Microstructure and mechanical properties of Y$_2$O$_3$ reinforced Ti6Al4V composites fabricated by spark plasma sintering. *J. Alloys Compd.* **2018**, *768*, 49–56. [CrossRef]

77. Liang, C.J.; Wang, C.L.; Zhang, K.X.; Liang, M.L.; Xie, Y.G.; Liu, W.J.; Yang, J.J.; Zhou, S.F. Nucleation and strengthening mechanism of laser cladding aluminum alloy by Ni-Cr-B-Si alloy powder based on rare earth control. *J. Mater. Process. Technol.* **2021**, *294*, 117145. [CrossRef]

78. Gao, Z.; Zhang, S.; Ren, C.; Yu, Y.; Gao, Z.; Zhang, C. Effect of rare-earth La$_2$O$_3$ on tribological properties of laser cladding nickel-based coatings on 35CrMoV alloy steel. *J. Mater. Eng. Perform.* **2023**, 1–9. [CrossRef]

79. Zhang, Z.; Yang, Q.; Yu, Z.; Wang, H.; Zhang, T. Influence of Y$_2$O$_3$ addition on the microstructure of TiC reinforced Ti-based composite coating prepared by laser cladding. *Mater. Charact.* **2022**, *189*, 111962. [CrossRef]

80. Li, Z.; Zhao, W.; Yu, K.; Guo, N.; Xiao, G.; Wang, Z.; Zhang, H. Effect of Y$_2$O$_3$ on microstructure and properties of CoCrFeNiTiNb high entropy alloy coating on Ti-6Al-4V surface by laser cladding. *J. Rare Earths* **2023**, *in press*. [CrossRef]

81. Guo, K.; Sun, Y.; Cheng, W. Effect of rare earth La$_2$O$_3$ on the microstructure and tribological properties of laser-clad CoCrFeNiMoSi high-entropy alloy coatings. *Mater. Lett.* **2024**, *355*, 135398. [CrossRef]

82. Wang, C.; Gao, Y.; Wang, R.; Wei, D.; Cai, M.; Fu, Y. Microstructure of laser-clad Ni60 cladding layers added with different amounts of rare-earth oxides on 6063 Al alloys. *J. Alloys Compd.* **2018**, *740*, 1099–1107. [CrossRef]

83. Yang, L.; Li, Z.; Zhang, Y.; Wei, S.; Wang, Y.; Kang, Y. In-situ TiC-Al$_3$Ti reinforced Al-Mg composites with Y$_2$O$_3$ addition formed by laser cladding on AZ91D. *Surf. Coat. Technol.* **2020**, *383*, 125249. [CrossRef]

84. Yongfu, X.; Dejun, K. Effect of La$_2$O$_3$ addition on microstructure and tribological performance of laser cladded Ni-WC coating on S136 steel. *Trans. Indian Inst. Met.* **2022**, *75*, 1843–1852. [CrossRef]

85. Gu, D.; Shen, Y.; Zhao, L.; Xiao, J.; Wu, P.; Zhu, Y. Effect of rare earth oxide addition on microstructures of ultra-fine WC-Co particulate reinforced Cu matrix composites prepared by direct laser sintering. *Mater. Sci. Eng. A* **2007**, *445–446*, 316–322. [CrossRef]

86. Zhang, Z.; Yang, F.; Zhang, H.; Zhang, T.; Wang, H.; Xu, Y.; Ma, Q. Influence of CeO$_2$ addition on forming quality and microstructure of TiC-reinforced CrTi$_4$-based laser cladding composite coating. *Mater. Charact.* **2021**, *171*, 110732. [CrossRef]

87. Zhang, T.; Feng, K.; Li, Z.; Kokawa, H. Effects of rare earth elements on the microstructure and wear properties of TiB$_2$ reinforced aluminum matrix composite coatings: Experiments and first principles calculations. *Appl. Surf. Sci.* **2020**, *530*, 147051. [CrossRef]

88. Jiang, Y.; Liu, F. Effects of Sc or/and Ge addition on microstructure and mechanical properties of as-cast 6016 Al alloy. *J. Alloys Compd.* **2019**, *809*, 151829. [CrossRef]

89. Lu, B.; Cui, X.; Ma, W.; Dong, M.; Fang, Y.; Wen, X.; Jin, G.; Zeng, D. Promoting the heterogeneous nucleation and the functional properties of directed energy deposited NiTi alloy by addition of La$_2$O$_3$. *Addit. Manuf.* **2020**, *33*, 101150. [CrossRef]

90. Tan, Q.; Yin, Y.; Fan, Z.; Zhang, J.; Liu, Y.; Zhang, M.-X. Uncovering the roles of LaB$_6$-nanoparticle inoculant in the AlSi10Mg alloy fabricated via selective laser melting. *Mater. Sci. Eng. A* **2021**, *800*, 140365. [CrossRef]

91. Bermingham, M.J.; StJohn, D.H.; Krynen, J.; Tedman-Jones, S.; Dargusch, M.S. Promoting the columnar to equiaxed transition and grain refinement of titanium alloys during additive manufacturing. *Acta Mater.* **2019**, *168*, 261–274. [CrossRef]

92. Zhang, D.; He, X.; Gao, Y.; Qin, B. Investigation of the microstructure and wear properties of laser clad Al-Si coatings containing different Y$_2$O$_3$ contents. *Coatings* **2023**, *13*, 308. [CrossRef]

93. Li, T.; Wang, X.T.; Tang, S.Q.; Yang, Y.S.; Wu, J.H.; Zhou, J.X. Improved wear resistance of biodegradable Mg-1.5Zn-0.6Zr alloy by Sc addition. *Rare Met.* **2021**, *40*, 2206–2212. [CrossRef]

94. Jayaraman, M.; Kumar, T.S.; Priyadharshini, G.S.; Kumar, J.S. Characterization of Y$_2$O$_3$ particles reinforced AA6082 aluminum matrix composites produced using friction stir processing. *Mater. Res. Express* **2019**, *6*, 086509.

95. Shi, Y.; Li, J.; Zhang, J.; Wen, B.; Li, L.; Wang, X.; Ren, S. Effect of La$_2$O$_3$ addition on wear properties of Ni60a/SiC coating using laser-cladding. *Opt. Laser Technol.* **2022**, *148*, 107640. [CrossRef]

96. Yu, S.; Cao, J.; Li, S.; Huang, H.; Li, X. The tribological and mechanical properties of PI/PAI/EP polymer coating under oil lubrication, seawater corrosion and dry sliding wear. *Polymers* **2023**, *15*, 1507. [CrossRef]

97. Zhang, Z.; Yang, Q.; Yang, F.; Zhang, H.; Zhang, T.; Wang, H.; Ma, Q. Comparative investigation on wear properties of composite coatings with varying CeO$_2$ contents. *Coatings* **2022**, *12*, 906. [CrossRef]

98. Wang, X.; Chen, C.; Zhang, M. Effect of heat treatment on microstructure and micro-wear resistance of selective laser melted Mg-Al-Zn alloy with La$_2$O$_3$ addition. *J. Mater. Eng. Perform.* **2021**, *30*, 2316–2328. [CrossRef]

99. Zheng, B.; He, T.; Yue, C.; Lin, X.; Yuan, X.; Dong, F.; Zhang, Y.; Huang, H.; Zuo, X.; Luo, L.; et al. Realization of synergistic enhancement for strength, wear resistance and ductility via adding La$_2$O$_3$ particles in (TiB+TiC)/Ti6Al4V composite. *Wear* **2023**, *526–527*, 204945. [CrossRef]

100. Xu, L.; Yan, H.; Liu, W.; Xiong, J. Effects of rare earth Pr/Ce on tribological behavior of ADC12 alloy. *J. Wuhan Univ. Technol.-Mater. Sci. Ed.* **2021**, *36*, 136–142. [CrossRef]

101. Sharma, V.K.; Kumar, V.; Joshi, R.S. Investigation of rare earth particulate on tribological and mechanical properties of Al-6061 alloy composites for aerospace application. *J. Mater. Res. Technol.* **2019**, *8*, 3504–3516. [CrossRef]

102. Wang, W.; Chen, Z.; Feng, S. Effect of CeO$_2$ on impact toughness and corrosion resistance of WC reinforced Al-based coating by laser cladding. *Materials* **2019**, *12*, 2901. [CrossRef] [PubMed]

103. Zhang, X.; Zhu, S.; Zhang, B.; Ahmad, T.; Wang, C.; Zhou, L.; Liang, T.; Yang, B. Effect of Y$_2$O$_3$ addition on the microstructure, wear resistance, and corrosion behavior of W-4.9Ni-2.1Fe heavy alloy. *J. Mater. Eng. Perform.* **2019**, *28*, 4801–4810. [CrossRef]

104. Gou, J.; Wang, Y.; Zhang, Y.; Wang, C.; Wang, G. Dry sliding wear behavior of Fe-Cr-C-B hardfacing alloy modified with nano-CeO$_2$ and its mechanisms of modification. *Wear* **2021**, *484–485*, 203756. [CrossRef]

105. Wu, T.; Li, Y.; Liu, G.; Zhao, H.; Wu, B. Effect of Yb$_2$O$_3$ and Tm$_2$O$_3$ on the wear resistance of high-alumina ceramics. *Wear* **2020**, *452–453*, 203281. [CrossRef]

106. Zhang, S.; Li, M.; Yoon, J.H.; Cho, T.Y.; Lee, C.G.; He, Y. The comparative study on microstructure and properties of nano-CeO$_2$ and Sm$_2$O$_3$ particulate reinforced nickel-based composites by laser deposition. *Appl. Surf. Sci.* **2008**, *254*, 7446–7452. [CrossRef]

107. Su, W.; Cui, X.; Jin, G.; Liu, C.; Liu, E.; Zhao, H.; Cao, B. Effects of different Y compounds on the microstructure and properties of laser cladding NiTi coatings in a semi-open environment. *Intermetallics* **2023**, *160*, 107936. [CrossRef]

108. Chan, S.; Hsueh, C. Effects of La addition on the microstructure and mechanical properties of CoCrNi medium entropy alloy. *J. Alloys Compd.* **2022**, *894*, 162401. [CrossRef]

109. Zhang, F.; Zhao, W.; Zhang, W.; Liao, Z.; Xiang, X.; Gou, H.; Li, Z.; Wei, H.; Wu, X.; Shan, Q. Microstructure, mechanical properties and wear resistance of rare earth doped WC/steel matrix composites: Experimental and calculations. *Ceram. Int.* **2023**, *49*, 2638–2647. [CrossRef]

110. Cao, F.; Zhang, X.; Jiang, Y.; Cai, P.; Li, Q.; Wang, T.; Dong, G.; Gao, F.; Liang, S. Effect of different rare earths on microstructures and tensile strength of in situ hybrid reinforced (TiB$_{2p}$ + TiBw)/Cu composites. *Mater. Charact.* **2022**, *184*, 111624. [CrossRef]

111. Liang, J.; Yin, X.; Lin, Z.; Chen, S.; Liu, C.; Yan, S.; Dong, S. Effects of LaB$_6$ on microstructure evolution and properties of in-situ synthetic TiC+TiBx reinforced titanium matrix composite coatings prepared by laser cladding. *Surf. Coat. Technol.* **2020**, *403*, 126409. [CrossRef]

112. Guo, Y.; Xu, Z.; Liu, Y.; Liu, M.; Sha, P.; Li, L.; Yu, Z.; Zhang, Z.; Ren, L. Achieving illustrious friction and corrosion resistance on a laser powder bed fusion nitinol rare earth alloy. *Mater. Today Adv.* **2023**, *17*, 100350. [CrossRef]

113. Sharma, V.; Kumar, V.; Joshi, R. Effect of RE addition on wear behavior of an Al-6061 based hybrid composite. *Wear* **2019**, *426–427*, 961–974. [CrossRef]

114. Du, J.; Li, F.; Li, Y.; Lu, H.; Qi, X.; Yang, B.; Li, C.; Yu, P.; Wang, J.; Gao, L. The influence of nano-CeO$_2$ on tribological properties and microstructure evolution of Cr$_3$C$_2$-NiCrCoMo composite coatings at high temperature. *Surf. Coat. Technol.* **2021**, *428*, 127913. [CrossRef]

115. Yue, J.; Liu, X.; Sui, Y.; Liu, C.; Sun, X.; Chen, W. Combined effect of Y$_2$O$_3$ nanoparticles and Si second-phase oxide on microstructure and wear resistance of plasma-clad steel coating. *Surf. Coat. Technol.* **2020**, *403*, 126348. [CrossRef]

116. Debta, M.K.; Masanta, M. Effect of nano-Y$_2$O$_3$ on the microstructure and wear behaviour of TIG cladded TiC-Co-nY$_2$O$_3$ coating. *Int. J. Refract. Met. Hard Mater.* **2023**, *111*, 106078. [CrossRef]

117. Wang, L.; Yang, L.; Huang, Y.; Yuan, Y.; Jia, C. Effects of Y$_2$O$_3$ addition on the microstructure and wear-resistant performance of TiN/TiB-reinforced Ti-based laser-clad coatings on Ti-6Al-4V alloys. *Mater. Today Commun.* **2021**, *29*, 102752. [CrossRef]

118. Zhang, T.; Zhuang, H.; Zhang, Q.; Yao, B.; Yang, F. Influence of Y$_2$O$_3$ on the microstructure and tribological properties of Ti-based wear-resistant laser-clad layers on TC4 alloy. *Ceram. Int.* **2020**, *46*, 13711–13723. [CrossRef]

119. Chauhan, H.R.; Saladi, S.; Variya, S.; Solanki, A.; Tailor, S.; Sooraj, K.P.; Ranjan, M.; Joshi, S. Role of micro- and nano-CeO$_2$ reinforcements on characteristics and tribological performance of HVOF sprayed Cr$_3$C$_2$-NiCr coatings. *Surf. Coat. Technol.* **2023**, *467*, 129684. [CrossRef]

120. Zhang, S.H.; Li, M.X.; Cho, T.Y.; Yoon, J.H.; Lee, C.G.; He, Y.Z. Laser clad Ni-base alloy added nano-and micron-size CeO$_2$ composites. *Opt. Laser Technol.* **2008**, *40*, 716–722. [CrossRef]

121. Weng, F.; Yu, H.; Chew, Y.; Bi, G.; Du, X.; Tian, H.; Chen, C. Microstructure and mechanical behavior of the laser synthesized composites modified by micro/nano scale rare earth oxides. *J. Alloys Compd.* **2022**, *895*, 162641. [CrossRef]

122. Sharma, V.K.; Kumar, V.; Joshi, R.S.; Sharma, D. Experimental analysis and characterization of SiC and RE oxides reinforced Al-6063 alloy based hybrid composites. *Int. J. Adv. Manuf. Technol.* **2020**, *108*, 1173–1187. [CrossRef]

123. Cao, F.; Dong, G.; Jiang, Y.; Xiao, P.; Wang, T.; Liang, S. Effect of La addition on microstructures and properties of TiB_2(-TiB)/Cu hybrid composites prepared by in situ reaction. *Mater. Sci. Eng. A* **2020**, *789*, 139605. [CrossRef]

124. Lu, B.; Cui, X.; Jin, G.; Dong, M.; Fang, Y.; Wen, X.; Ma, W. Effect of La_2O_3 addition on mechanical properties and wear behaviour of NiTi alloy fabricated by direct metal deposition. *Opt. Laser Technol.* **2020**, *129*, 106290. [CrossRef]

125. Cui, C.; Wu, M.; He, R.; Jie, D.; Gong, Y.; Miao, X. Effect of LaB_6 doping on the microstructure, microhardness and corrosion behavior of laser cladded FeCoNiCrMo coating on Ti6Al4V. *Surf. Coat. Technol.* **2023**, *466*, 129592. [CrossRef]

126. Zhang, Z.; Yang, Q.; Yu, Z.; Zhang, T.; Jing, J. Microstructure and performance of Ti-based wear-resistant laser cladding coatings with rare-earth oxides. *Mater. Lett.* **2023**, *350*, 134856. [CrossRef]

127. Xu, Z.; Guo, Y.; Liu, Y.; Sha, P.; Zhang, J.; Liang, P.; Yu, Z.; Zhang, Z.; Ren, L. Anti-tribocorrosion resistance of NiTi–CeO_2 alloys fabricated by laser powder bed fusion. *Compos. Commun.* **2023**, *38*, 101512. [CrossRef]

128. Bhoi, N.K.; Singh, H.; Pratap, S.; Jain, P.K. Aluminum yttrium oxide metal matrix composite synthesized by microwave hybrid sintering: Processing, microstructure and mechanical response. *J. Inorg. Organomet. Polym. Mater.* **2022**, *32*, 1319–1333. [CrossRef]

129. Yi, X.; Sun, K.; Wang, H.; Gong, Y.; Meng, X.; Gao, Z.; Zhang, H.; Cai, W. Tuning microstructure, transformation behavior, mechanical/functional properties of Ti-V-Al shape memory alloy by doping quaternary rare earth Y. *Prog. Nat. Sci. Mater. Int.* **2021**, *31*, 296–302. [CrossRef]

130. Xu, Z.; Guo, Y.; Liu, Y.; Yu, Z.; Zhang, Z.; Ren, L. The martensitic transformation behavior and shape memory effect of laser powder bed fusion NiTi alloys influenced by rare earth addition. *Mater. Sci. Eng. A* **2022**, *848*, 143350. [CrossRef]

131. Zhang, L.J.; Zhang, M.D.; Zhou, Z.; Fan, J.T.; Cui, P.; Yu, P.F.; Jing, Q.; Ma, M.Z.; Liaw, P.K.; Li, G.; et al. Effects of rare-earth element, Y, additions on the microstructure and mechanical properties of CoCrFeNi high entropy alloy. *Mater. Sci. Eng. A* **2018**, *725*, 437–446. [CrossRef]

132. Hu, J.; Liu, Y.; Zhao, X.; Xie, Y.; Li, W. Effects of TiC/CeO_2 addition on microstructure and wear resistance of Ni-based composite coatings fabricated by laser cladding on H13 steel. *Appl. Phys. A* **2019**, *125*, 1–9.

133. Cui, C.; Wu, M.; Miao, X.; Zhao, Z.; Gong, Y. Microstructure and corrosion behavior of CeO_2/FeCoNiCrMo high-entropy alloy coating prepared by laser cladding. *J. Alloys Compd.* **2022**, *890*, 161826. [CrossRef]

134. Shu, D.; Cui, X.; Li, Z.; Sun, J.; Wang, J.; Chen, X.; Dai, S.; Si, W. Effect of the rare earth oxide CeO_2 on the microstructure and properties of the nano-WC-reinforced Ni-based composite coating. *Metals* **2020**, *10*, 383. [CrossRef]

135. Zhao, Q.; Luo, H.; Pan, Z.; Wang, X.; Cheng, H.; Zong, Y. Effect of ion nitriding on properties of high carbon chromium bearing steel containing rare earth elements. *J. Mater. Eng. Perform.* **2023**, 1–12. [CrossRef]

136. Ai, X.; Liu, Z.; Zou, Z.; Wang, Z. Effect of nano-Y_2O_3 on the microstructure and properties of WC-reinforced Ni-based composite surfacing layer. *Materials* **2022**, *15*, 1665. [CrossRef]

137. Kumar, R.; Das, A.K. Effect of rare earth oxide (Y_2O_3) addition on wear characteristic of TiB_2 ceramic reinforced Mo-based composite coating fabricated by Argon shielded Arc cladding. *Phys. Scr.* **2023**, *98*, 085904. [CrossRef]

138. Jia, D.; Shi, W.; Zhang, H.; Wu, T.; Diao, Y.; Li, K.; Lu, C. Effects of Y_2O_3 content on wear resistance and corrosion resistance of 316L/TiC coating fabricated by laser cladding. *Coatings* **2023**, *13*, 1348. [CrossRef]

139. Das, A.K.; Kumar, R. Investigation on wear behaviour of TiC/Co/Y_2O_3 metal matrix composite coating developed on AZ91D Mg alloy by plasma transferred arc cladding process. *Mater. Lett.* **2024**, *355*, 135457. [CrossRef]

140. Wang, H.; Chen, T.; Cong, W.; Liu, D. Laser cladding of Ti-based ceramic coatings on Ti6Al4V alloy: Effects of CeO_2 nanoparticles additive on wear performance. *Coatings* **2019**, *9*, 109. [CrossRef]

141. Wang, X.H.; Liu, S.S.; Zhang, M.; Qu, K.L. Effect of rare earth oxide on the microstructure and wear properties of in situ-synthesized ceramics-reinforced Fe-based laser cladding coatings. *Tribol. Trans.* **2020**, *63*, 345–355. [CrossRef]

142. Sharma, V.K.; Kumar, V.; Joshi, R.S. Experimental investigation on effect of RE oxides addition on tribological and mechanical properties of Al-6063 based hybrid composites. *Mater. Res. Express* **2019**, *6*, 865. [CrossRef]

143. Zhuang, H.; Zhang, Q.; Zhang, D. Microstructure and tribological properties of Ni-based laser-clad coatings by rare earth modification. *J. Therm. Spray Technol.* **2021**, *30*, 1410–1431. [CrossRef]

144. Liu, J.; Chen, T.; Duan, H.; Yuan, C.; Bai, X. Mechanical properties and cavitation erosion behavior of CeO_2-modified dual-scale WC-10Co-4Cr coating prepared by HVOF. *J. Therm. Spray Technol.* **2022**, *31*, 2463–2475. [CrossRef]

145. Chen, L.; Chen, W.; Li, D.; Jing, P.; Yin, H.; Wu, H.; Xie, Y.; Wang, X. Effect of nano-La_2O_3 doping on the tribological behavior of laser cladded WC-12Co coating on 65Mn steel under water lubrication condition. *Tribol. Int.* **2022**, *169*, 107428. [CrossRef]

146. Cai, H.; Xue, Y.; Pang, B.; Wang, J.; Ye, J. Effect of rare earth La on friction and wear resistance of WS_2-based composite coating at high temperature. *J. Mater. Sci.* **2022**, *57*, 16875–16891. [CrossRef]

147. Yu, X.; Yao, M.; Xue, J.; Lei, J. Effect of CeO_2 on the elevated-temperature wear behaviour of in situ TiB_2/A356 composite. *Mater. Sci. Technol.* **2021**, *37*, 1002–1013. [CrossRef]

148. Han, B.; Lin, J.; Han, X.; Wang, H.; Cui, W. Effect of CeO_2 on high-temperature wear resistance of WC/Fe-based coatings. *Surf. Eng.* **2021**, *37*, 982–990. [CrossRef]

149. Liu, Y.; Yang, G.; Hang, Z.; Fu, H.; Xi, N.; Chen, H. Elevated temperature wear behaviour of CeO_2 modified WC-12Co coating. *J. Rare Earths* **2019**, *37*, 673–678. [CrossRef]

150. Chen, J.-X.; Yang, Y.; Etim, I.P.; Tan, L.-L.; Yang, K.; Misra, R.; Wang, J.-H.; Su, X.-P. In vitro degradation, wear property and biocompatibility of nano-Y_2O_3-containing micro-arc oxidation coating on ZK60 alloy. *Trans. Nonferrous Met. Soc. China* **2023**, *33*, 1411–1424. [CrossRef]

151. Tong, X.; Sun, Q.; Zhang, D.; Wang, K.; Dai, Y.; Shi, Z.; Li, Y.; Dargusch, M.; Huang, S.; Ma, J.; et al. Impact of scandium on mechanical properties, corrosion behavior, friction and wear performance, and cytotoxicity of a β-type Ti-24Nb-38Zr-2Mo alloy for orthopedic applications. *Acta Biomater.* **2021**, *134*, 791–803. [CrossRef] [PubMed]

152. Shaikh, S.; Omiya, T.; Cavaleiro, A.; Vilhena, L.; Ramalho, A.; Ferreira, F. Impact of temperature variation on friction behaviour of rare earth-doped diamond-like carbon coatings with ionic liquid lubricants. *Lubricants* **2023**, *11*, 302. [CrossRef]

153. Xiang, D.; Tan, X.; Sui, X.; He, J.; Chen, C.; Hao, J.; Liao, Z.; Liu, W. Comparative study on microstructure, bio-tribological behavior and cytocompatibility of Cr-doped amorphous carbon films for Co-Cr-Mo artificial lumbar disc. *Tribol. Int.* **2021**, *155*, 106760. [CrossRef]

154. Xiang, D.D.; Sui, X.D.; Tan, X.P.; Hao, J.Y.; Wang, Z.W.; Liao, Z.H.; Liu, W.Q.; Tor, S.B. Improving biotribological properties and corrosion resistance of CoCrMo alloy via a Cr-GLC nanocomposite film in simulated body fluids. *Surf. Coat. Technol.* **2019**, *378*, 124840. [CrossRef]

155. Xiao, Y.; Sun, W.C.; Ma, M.; Jia, Y.P.; Liu, J.P.; Zhang, T.Q. Microstructure, wear and corrosion behavior of nano-CeO_2 doped diamond-like carbon (DLC) composite films. *Diam. Relat. Mater.* **2022**, *126*, 109087. [CrossRef]

156. Liu, J.; Long, X.; Zhu, H.; Zhu, W.; Chen, Z.; He, D.; Song, N.; Wang, X. Effects of La_2O_3 contents on microstructure and properties of laser-cladded 5 wt% CaB_6/HA bioceramic coating. *Biomed. Mater.* **2022**, *17*, 025007. [CrossRef]